

Refining the properties of the TOI-178 system with CHEOPS and TESS ^{★,★★}

L. Delrez^{1,2}, A. Leleu^{3,4}, A. Brandeker⁵, M. Gillon¹, M. J. Hooton^{6,4}, A. Collier Cameron⁷, A. Deline³, A. Fortier^{4,8}, D. Queloz^{9,6}, A. Bonfanti¹⁰, V. Van Grootel², T. G. Wilson⁷, J. A. Egger⁴, Y. Alibert⁴, R. Alonso^{11,12}, G. Anglada^{13,14}, J. Asquier¹⁵, T. Bárczy¹⁶, D. Barrado y Navascues¹⁷, S. C. C. Barros^{18,19}, W. Baumjohann¹⁰, M. Beck³, T. Beck⁴, W. Benz^{4,8}, N. Billot³, X. Bonfils²⁰, L. Borsato²¹, C. Broeg^{4,8}, M. Buder²², J. Cabrera²³, V. Cessa⁴, S. Charnoz²⁴, Sz. Csizmadia²³, P. E. Cubillos^{25,10}, M. B. Davies²⁶, M. Deleuil²⁷, O. D. S. Demangeon^{18,19}, B.-O. Demory^{8,4}, D. Ehrenreich^{3,28}, A. Erikson²³, L. Fossati¹⁰, M. Fridlund^{29,30}, D. Gandolfi³¹, M. Güdel³², J. Hasiba¹⁰, S. Hoyer²⁷, K. G. Isaak³³, J. M. Jenkins³⁴, L. L. Kiss^{35,36}, J. Laskar³⁷, D. W. Latham³⁸, A. Lecavelier des Etangs³⁹, M. Lendl³, C. Lovis³, R. Luque⁴⁰, D. Magrin²¹, P. F. L. Maxted⁴¹, C. Mordasini^{4,8}, V. Nascimbeni²¹, G. Olofsson⁵, R. Ottensamer⁴², I. Pagano⁴³, E. Pallé¹¹, G. Peter²², G. Piotto^{21,44}, D. Pollacco⁴⁵, R. Ragazzoni^{21,44}, N. Rando¹⁵, H. Rauer^{23,46,47}, I. Ribas^{13,14}, G. Ricker^{48,49}, N. C. Santos^{18,19}, G. Scandariato⁴³, S. Seager^{50,48,49,51}, D. Ségransan³, A. E. Simon⁴, A. M. S. Smith²³, S. G. Sousa¹⁸, M. Steller¹⁰, Gy. M. Szabó^{52,53}, N. Thomas⁴, S. Udry³, R. Vanderspek⁴⁸, J. Venturini³, V. Viotto²¹, N. A. Walton⁵⁴, J. N. Winn⁵⁵

(Affiliations can be found after the references)

Received ...; accepted ...

ABSTRACT

Context. The TOI-178 system consists of a nearby late K-dwarf transited by six planets in the super-Earth to mini-Neptune regime, with radii ranging from ~ 1.1 to $2.9 R_{\oplus}$ and orbital periods between 1.9 and 20.7 days. All planets but the innermost one form a chain of Laplace resonances. Mass estimates derived from a preliminary radial velocity (RV) dataset suggest that the planetary densities do not decrease in a monotonic way with the orbital distance to the star, contrary to what one would expect based on simple formation and evolution models.

Aims. To improve the characterisation of this key system and prepare for future studies (in particular with JWST), we perform a detailed photometric study based on 40 new CHEOPS visits, one new TESS sector, as well as previously published CHEOPS, TESS, and NGTS data.

Methods. First we update the parameters of the host star using the new parallax from *Gaia* EDR3. We then perform a global analysis of the 100 transits contained in our data to refine the physical and orbital parameters of the six planets and study their transit timing variations (TTVs). We also use our extensive dataset to place constraints on the radii and orbital periods of potential additional transiting planets in the system.

Results. Our analysis significantly refines the transit parameters of the six planets, most notably their radii, for which we now obtain relative precisions $\lesssim 3\%$, with the exception of the smallest planet *b* for which the precision is 5.1%. Combined with the RV mass estimates, the measured TTVs allow us to constrain the eccentricities of planets *c* to *g*, which are found to be all below 0.02, as expected from stability requirements. Taken alone, the TTVs also suggest a higher mass for planet *d* than the one estimated from the RVs, which had been found to yield a surprisingly low density for this planet. However, the masses derived from the current TTV dataset are very prior-dependent and further observations, over a longer temporal baseline, are needed to deepen our understanding of this iconic planetary system.

Key words. Planetary systems – Stars: individual: TOI-178 – Techniques: photometric

1. Introduction

Studying the relation between the internal composition of planets found in multi-planet systems and their architecture (i.e. orbital properties) is crucial to improve our understanding of the formation and evolution of planetary systems. In this context,

* The photometric data used in this work are only available at the CDS via anonymous ftp to cdsarc.cds.unistra.fr (ftp://130.79.128.5) or via <https://cdsarc.cds.unistra.fr/viz-bin/cat/J/A+A/>

** This study uses CHEOPS data observed as part of the Guaranteed Time Observation (GTO) programme CH_PR100031.

planetary systems forming chains of three-body Laplace resonances, where each consecutive pair of planets are in (or close to) a mean-motion resonance (MMR), are of particular interest. Indeed, the fine-tuning and fragility of such orbital configurations ensure that no significant scattering or collision event has taken place since the formation of the planets in the protoplanetary disc (e.g. Mills et al. 2016). Hence, these systems are real goldmines for constraining the outcome of protoplanetary discs and provide important anchors for planet formation models.

To date, chains of Laplace resonances have only been observed for a few systems: GJ 876 (Rivera et al. 2010), Kepler-60 (Goździewski et al. 2016), Kepler-80 (MacDonald et al. 2016),

Kepler-223 (Mills et al. 2016), TRAPPIST-1 (Gillon et al. 2017; Luger et al. 2017), K2-138 (Christiansen et al. 2018; Lopez et al. 2019), TOI-178 (Leleu et al. 2021a, hereafter L21), and TOI-1136 (Dai et al. 2023). All these systems, except GJ 876, are transiting, which provides an opportunity to constrain the masses and eccentricities of the planets via their transit timing variations (TTVs), which may have detectable amplitudes thanks to the proximity of each pair of planets to a MMR. For stars that are bright enough, it is also possible to obtain radial velocity (RV) measurements, that can provide complementary constraints on the planetary masses and orbital parameters. Out of the transiting systems cited above, only K2-138, TOI-1136, and TOI-178 have published RV measurements so far, the other ones being too faint in the visible ($V\text{-mag} \geq 14$). In this work, we focus on the latter of these three systems.

The nearby (~ 63 pc) late K-type star TOI-178 was initially flagged by the *Transiting Exoplanet Survey Satellite* (TESS, Ricker et al. 2015) as a potential host to three transiting sub-Neptunes with orbital periods of 6.56, 9.96, and 10.35 days, based on data from its Sector 2. The 0.4-day difference in the orbital periods of the two outer planetary candidates led Leleu et al. (2019) to hypothesise that they occupied a horseshoe orbital configuration. Thanks to an intensive photometric follow-up with the *CHaracterising ExOPlanets Satellite* (CHEOPS, Benz et al. 2021), L21 demonstrated that this was actually not the case, and revealed instead a compact system of at least six transiting planets in the super-Earth to mini-Neptune regime, with radii ranging from ~ 1.1 to $2.9 R_{\oplus}$ and orbital periods of 1.91, 3.24, 6.56, 9.96, 15.23, and 20.71 days. The five outer planets form a 2:4:6:9:12 chain of Laplace resonances, while the innermost planet b lies just outside the 3:5 MMR with planet c , which could indicate that it was previously part of the chain but was then pulled away, possibly by tidal forces.

Using RV measurements obtained with the Echelle SPectrograph for Rocky Exoplanets and Stable Spectroscopic Observations (ESPRESSO, Pepe et al. 2021) installed at ESO's Very Large Telescope, L21 were also able to derive preliminary estimates for the masses of the planets, and thus their bulk densities (when combined with the radii inferred from the transit photometry). The planetary densities that they found show important variations from planet to planet, jumping for example from ~ 1 to $0.2 \rho_{\oplus}$ between planets c and d . By doing a Bayesian internal structure analysis, they showed that the two innermost planets are likely to be mostly rocky, which could indicate that they have lost their primordial gas envelope through atmospheric escape, while all the other planets appear to contain significant amounts of water and/or gas (see also the independent internal structure analysis by Acuña et al. 2022). Interestingly, it seems that the amount of gas in the planets does not vary as a monotonic function of the orbital distance to the star, as opposed to what one would expect from simple formation and evolution models and unlike other known systems in a chain of Laplace resonances. The most notable outlier is planet d , which seems to have a larger gas mass than planet e (with a probability of 92%), although the latter is more massive and at a larger distance from the star. This is surprising for two reasons. First, from a formation perspective, one would expect that the mass of the primordial gas envelope is a growing function of the total planetary mass. Second, from an evolution point of view, one would also expect that atmospheric evaporation is more effective for planets that are closer to the star. Based on these considerations, we would thus expect planet d to have a smaller gas mass than planet e . Another possible outlier is planet f , which appears to be the most massive planet in the system, but may still have less gas than planet e (with a

probability of $\sim 60\%$) despite being located further away from the star.

However, the planetary densities on which these results are based are rather poorly constrained (precision $\geq 30\%$). In particular, the planetary masses presented by L21 were derived using only 46 RV data points, a very limited dataset for such a complex system. Further RV observations are thus needed to confirm and refine these preliminary mass estimates. Complementary constraints on the masses and eccentricities of the planets could also be obtained by monitoring their TTVs, which are expected to be measurable for all but the innermost planet, with predicted amplitudes ranging from a few minutes for the inner planets to a few tens of minutes for the outer ones (L21). Such transit follow-up observations would also be useful to refine the transit parameters of the planets and their radii. Improving the overall characterisation of the TOI-178 system is essential to optimally prepare the atmospheric follow-up observations that are scheduled on JWST/NIRSpec (PI: M. Hooton) for three of its planets (b , d , and g) and support the interpretation of the resulting transmission spectra.

These considerations motivated the work presented here, which consists in a detailed photometric study of the TOI-178 system, based on 40 new CHEOPS visits, one new TESS sector, as well as previously published data. Our extensive dataset contains 100 transits of the six planets in total, about twice more than the transit dataset presented in L21. The paper is structured as follows. In Sect. 2, we update the properties of the host star using the new parallax from *Gaia* EDR3. Sect. 3 describes all the observations that we used in our work, with a particular focus on the new data presented in this paper. In Sect. 4, we present our detailed analysis of all these data, including a global transit analysis to refine the system parameters and measure the individual transit timings (Sect. 4.1), as well as a search for possible additional transiting planets in the data and an assessment of their detection limits (Sect. 4.2). In Sect. 5, we present a dynamical analysis of the individual transit timings measured for the five outer planets, before concluding in Sect. 6.

2. Stellar properties

L21 already provided a thorough characterisation of the host star. Table 1 gives the effective temperature (T_{eff}), surface gravity ($\log g_{\star}$), metallicity ($[\text{Fe}/\text{H}]$), and projected rotational velocity ($v \sin i_{\star}$) that they derived from a detailed spectroscopic analysis of the 46 ESPRESSO high-resolution spectra. We refine here the stellar radius of TOI-178 in a similar fashion as in L21, but using updated *Gaia* EDR3 photometry and parallax values. In brief, we employed a Markov-Chain Monte Carlo (MCMC) modified infrared flux method (IRFM; Blackwell & Shallis 1977; Schanche et al. 2020) to compute the bolometric flux by fitting *Gaia* (Gaia Collaboration et al. 2021), 2MASS (Skrutskie et al. 2006), and WISE (Wright et al. 2010) broadband photometry with stellar atmospheric models (Castelli & Kurucz 2003). In this process, the spectroscopic parameters from L21 were used as priors on stellar atmospheric model selection. The bolometric flux was then converted into stellar effective temperature and angular diameter, which was subsequently used to determine the stellar radius (R_{\star}) of TOI-178 using the offset-corrected *Gaia* EDR3 parallax (Lindgren et al. 2021). Via this method, we obtained $R_{\star} = 0.662 \pm 0.010 R_{\odot}$, which is similar to the value reported in L21.

Taking advantage of the R_{\star} revision, we re-derived the isochronal mass (M_{\star}) and age (t_{\star}) following the same procedure outlined in L21. We inputted $[\text{Fe}/\text{H}]$, T_{eff} , and R_{\star} into two

Table 1. Updated properties of the host star TOI-178.

Property (unit)	Value	Source
<i>Astrometric properties</i>		
RA (J2000)	00:29:12.49	[1]
Dec (J2000)	−30:27:14.86	[1]
μ_{RA} (mas yr ^{−1})	150.032 ± 0.028	[1]
μ_{Dec} (mas yr ^{−1})	−87.132 ± 0.030	[1]
Parallax (mas)	15.900 ± 0.031	[1]
Distance (pc)	62.89 ± 0.12	from parallax
<i>Photometric magnitudes</i>		
G (mag)	11.1575 ± 0.0028	[1]
G_{BP} (mag)	11.8398 ± 0.0029	[1]
G_{RP} (mag)	10.3602 ± 0.0038	[1]
J (mag)	9.372 ± 0.021	[2]
H (mag)	8.761 ± 0.023	[2]
K (mag)	8.656 ± 0.021	[2]
$W1$ (mag)	8.573 ± 0.022	[3]
$W2$ (mag)	8.64 ± 0.02	[3]
<i>Spectroscopic and derived properties</i>		
T_{eff} (K)	4316 ± 70	Spectroscopy [4]
$\log g_{\star}$ (cgs)	4.45 ± 0.15	Spectroscopy [4]
[Fe/H] (dex)	−0.23 ± 0.05	Spectroscopy [4]
$v \sin i_{\star}$ (km s ^{−1})	1.5 ± 0.3	Spectroscopy [4]
R_{\star} (R_{\odot})	0.662 ± 0.010	IRFM [5]
M_{\star} (M_{\odot})	0.647 ^{+0.030} _{−0.029}	Isochrones [5]
t_{\star} (Gyr)	6.0 ^{+6.8} _{−5.0}	Isochrones [5]
L_{\star} (L_{\odot})	0.136 ± 0.010	from R_{\star} and T_{eff} [5]
ρ_{\star} (ρ_{\odot})	2.23 ± 0.14	from R_{\star} and M_{\star} [5]

References. [1] *Gaia* EDR3 (Gaia Collaboration et al. 2021); [2] 2MASS (Skrutskie et al. 2006); [3] WISE (Wright et al. 2010); [4] Leleu et al. (2021a); [5] this work (see Sect. 2).

different stellar evolutionary models, namely PARSEC¹ v1.2S (Marigo et al. 2017) and CLES (Code Liégeois d’Évolution Stellaire, Scuflaire et al. 2008) to obtain two pairs of mass and age estimates. In particular, the first pair ($M_{\star,1}$, $t_{\star,1}$) was computed by the isochrone placement algorithm (Bonfanti et al. 2015, 2016), which interpolates the provided input values within pre-computed grids of PARSEC isochrones and tracks. The routine convergence was further aided by the $v \sin i_{\star}$ -based gyrochronological relation (with $v \sin i_{\star}$ the projected rotational velocity) implemented within the isochrone placement, as described in Bonfanti et al. (2016). The second pair ($M_{\star,2}$, $t_{\star,2}$), instead, was retrieved by CLES, which generates the best-fit ‘on-the-fly’ stellar track, following the Levenberg-Marquardt minimisation scheme presented in Salmon et al. (2021). After carefully checking the mutual consistency of the two respective pairs of outcomes through the χ^2 -based criterion broadly discussed in Bonfanti et al. (2021), we finally merged the two results and obtained $M_{\star} = 0.647^{+0.030}_{-0.029} M_{\odot}$ and $t_{\star} = 6.0^{+6.8}_{-5.0}$ Gyr. Those values are similar to those reported in L21. Our revised stellar parameters are presented at the bottom of Table 1.

3. Data

In this section, we describe all the photometric data that we used in our work. Table 2 summarises the number of transits obtained

¹ PAdova and TRieste Stellar Evolutionary Code: <http://stev.oapd.inaf.it/cgi-bin/cmd>

for each planet and facility, with a total of 100 transits observed for the system. This is about twice more than the transit dataset presented in L21.

Table 2. Number of transits observed for each planet and facility.

Facility	Planet					
	b	c	d	e	f	g
CHEOPS	19	9	5	4	4	4
TESS	23	14	6	4	4	2
NGTS	1	–	–	–	–	1
Total number of transits	43	23	11	8	8	7

3.1. CHEOPS

We obtained 44 visits (observation runs) of TOI-178 with CHEOPS (Benz et al. 2021) in total, of which only four were presented previously in L21. These observations were acquired between 21 July 2020 and 18 October 2021 as part of the Guaranteed Time Observations (GTO) program and are summarised in Table A.1. Since CHEOPS revolves around the Earth on a low-altitude (~700 km) Sun-synchronous orbit, the data show some interruptions corresponding to occultations of the target by the Earth or passages through the South Atlantic Anomaly (SAA). For our TOI-178 visits, the resulting observing efficiencies (fraction of time used for science observations) vary between 45 and 93% depending on the date of observation. Due to the relative faintness of TOI-178 (G -mag=11.15) for CHEOPS, we used the maximum exposure time of 60 seconds for all visits.

As part of our CHEOPS dataset is the near-continuous 11-day observation performed in August 2020, split into two visits for scheduling reasons, that was previously presented in L21. Among the other 42 visits, 23 of them were scheduled to cover transits of the known planets, while the remaining 19 were ‘fillers’, i.e. observations that are carried out when CHEOPS has no time-constrained or higher-priority observations. In the case of TOI-178, the goal of these fillers was to search for other potential transiting planets in the system but they did not reveal any transit-like signal (see Sect. 4.2). Together, the CHEOPS data covered 19, 9, 5, 4, 4, and 4 transits of TOI-178 b, c, d, e, f, and g, respectively.

The raw data of each visit were automatically processed with the CHEOPS Data Reduction Pipeline (DRP version 13.1.0; Hoyer et al. 2020). In short, the DRP calibrates the raw images (event flagging, bias and gain corrections, linearisation, dark current, and flat field corrections), corrects them for environmental effects (cosmic rays, background, and smearing trails from nearby stars), and performs aperture photometry to extract the target’s flux for four different apertures. Using the *pycheops* package² (Maxted et al. 2022) to analyse the different light curves, we found that the best precision is obtained in this case with the default photometric aperture (25 pixels). Owing to the extended and irregular shape of the CHEOPS Point Spread Function (PSF) and the fact that the field rotates around the target along the spacecraft’s nadir-locked orbit (Benz et al. 2021), nearby background stars can introduce time-variable flux contamination in the photometric aperture, in phase with the spacecraft roll angle (see e.g. Lendl et al. 2020; Bonfanti et al. 2021;

² <https://github.com/pmated/pycheops>

Maxted et al. 2022). The DRP also provides an estimation of this contamination by using *Gaia* DR2 catalogue (Gaia Collaboration et al. 2018) and a PSF template to simulate CHEOPS images of the field of view. For our TOI-178 observations, this contamination varies between 0.03 and 0.09% of the target’s flux and is mostly modulated by the rotation around the target of a nearby background star with G -mag=13.3 at a projected sky distance of 60.8". The light curves were corrected for this contamination.

To get an independent photometric extraction, we also reduced the data with PIPE³ (Brandeker et al. in prep., Morris et al. 2021, Szabó et al. 2021, Deline et al. 2022, Brandeker et al. 2022), a PSF photometry package developed specifically for CHEOPS that has demonstrated an improved precision for faint stars (G -mag ≥ 11) such as TOI-178 in a previous work (Morris et al. 2021). PIPE first uses a principal component analysis (PCA) approach to derive a PSF template library from the data series. The first five principal components (PCs) together with a constant background are then used to fit the individual PSFs of each image using a least-squares minimisation and measure the target’s flux. The number of PCs to use is a trade-off between following systematic PSF changes and overfitting the noise. For faint stars such as TOI-178, the mean PSF (first PC) is sufficient for a good extraction, and attempts to model the PSF better with more PCs usually introduce noise in the extracted light curve. Some advantages of using PSF photometry rather than aperture photometry for faint targets are that: (1) the contributions to the signal of each pixel over the PSF are weighted according to noise so that higher S/N photometry can be extracted; (2) cosmic rays and bad pixels (both hot and telegraphic) are easier to filter out or give lower weight in the fitting process; (3) PSF photometry is less sensitive to contamination from nearby background stars; (4) the background is fit simultaneously with the PSF for the same pixels, which can be an advantage if there is some spatial structure.

For each visit, we estimated the photometric precision by computing the median absolute deviation (MAD) of the difference between two consecutive data points ($df = f_{i+1} - f_i$) of the light curve. This metric is robust to outliers and removes correlated signals (e.g. transits). Table A.1 gives the MAD that we obtained for both the DRP and PIPE. We found a significant improvement for PIPE, of 18% on average in terms of MAD. We thus decided to use the PIPE light curves in our global analysis.

3.2. TESS

TESS (Ricker et al. 2015) observed TOI-178 for the first time during Cycle 1/Sector 2 of its primary mission (22 August – 20 September 2018). These data, obtained with a two-minute cadence, were previously presented in L21 and we include them in our global analysis. TESS observed again TOI-178 during Cycle 3/Sector 29 of its extended mission, from 26 August to 22 September 2020. The observations were acquired on CCD 3 of camera 2. The data were processed with the TESS Science Processing Operations Center (SPOC) pipeline (Jenkins et al. 2016) at NASA Ames Research Center. We retrieved the 2-minute cadence Presearch Data Conditioning Simple Aperture Photometry (PDCSAP, Stumpe et al. 2012; Smith et al. 2012; Stumpe et al. 2014) from the Mikulski Archive for Space Telescopes⁴ (MAST), using the default quality bitmask. Together, the two TESS sectors covered 23, 14, 6, 4, 4, and 2 transits of TOI-178 b, c, d, e, f, and g, respectively.

³ <https://github.com/alphapsa/PIPE>

⁴ <https://archive.stsci.edu>

3.3. NGTS

We also included in our global analysis the light curves obtained with the Next Generation Transit Survey (NGTS, Wheatley et al. 2018) that were previously published in L21: one transit of planet *b* observed simultaneously with six telescopes on 11 September 2019 and one transit of planet *g* observed on 12 October 2019 using seven telescopes, thus a total of 13 light curves. We refer the reader to L21 and references therein for more information about these NGTS data and their reduction.

4. Data analysis

4.1. Global transit analysis

We performed a joint fit of all the transit photometry described in Sect. 3 using the most recent version of the adaptive MCMC algorithm presented in Gillon et al. (2012, see also Gillon et al. 2014). In order to reduce processing times in this global transit analysis, we only used the portions of the data which contain transits (leaving enough out-of-transit data for proper modelling of the photometric baseline, see below), thus ending up with a total of 96 light curves (summarised in Table B.1). These light curves were modelled using the quadratic limb-darkening transit model of Mandel & Agol (2002) multiplied by a photometric baseline model, different for each light curve, aimed at representing the photometric variations caused by other astrophysical, instrumental, or environmental effects. For each light curve, we explored a large range of baseline models, including polynomials, cubic splines, or Gaussian Processes with respect to e.g. time, background, target’s location on the detector, spacecraft roll angle, telescope tube temperature (for CHEOPS), airmass (for NGTS), or combinations of these parameters. Table B.1 gives the baseline models selected for each light curve based on the Bayesian Information Criterion (BIC, Schwarz 1978). The minimal baseline model is a simple constant to account for any out-of-transit flux offset.

The model parameters sampled by the MCMC were:

- for each planet, the transit depth ($dF = R_p^2/R_\star^2$ where R_p is the radius of the planet and R_\star is the stellar radius) and the cosine of the orbital inclination ($\cos i_p$);
- the log of the stellar density ($\log \rho_\star$), the log of the stellar mass ($\log M_\star$), and the effective temperature (T_{eff});
- for the five outer planets, the transit timing variation (TTV, in minutes) of each transit with respect to the transit ephemerides defined by the orbital period (P) and the mid-transit time (T_0) reported in Tables 3 and 4 of L21;
- the log of the orbital period ($\log P$) and the mid-transit time (T_0) of TOI-178 b (we assumed a linear transit ephemeris for this planet as it is not part of the Laplace resonant chain and is thus not expected to show any significant TTVs, see L21);
- for each bandpass (CHEOPS, TESS, and NGTS), the combinations $q_1 = (u_1 + u_2)^2$ and $q_2 = 0.5 u_1(u_1 + u_2)^{-1}$ of the quadratic limb-darkening coefficients (u_1 and u_2), following the triangular sampling scheme advocated by Kipping (2013).

We note that our model thus did not include dynamical interactions between the components of the TOI-178 system; it assumed that there are no mutual interactions between the planets (fixed orbital periods) and then measured TTVs with respect to that Keplerian model. We also assumed circular orbits for all the planets (as justified in Sect. 5, see also L21) and thus set their respective $\sqrt{e} \cos \omega$ and $\sqrt{e} \sin \omega$ values (with e the eccentricity and ω the argument of periastron) to zero. Given the large

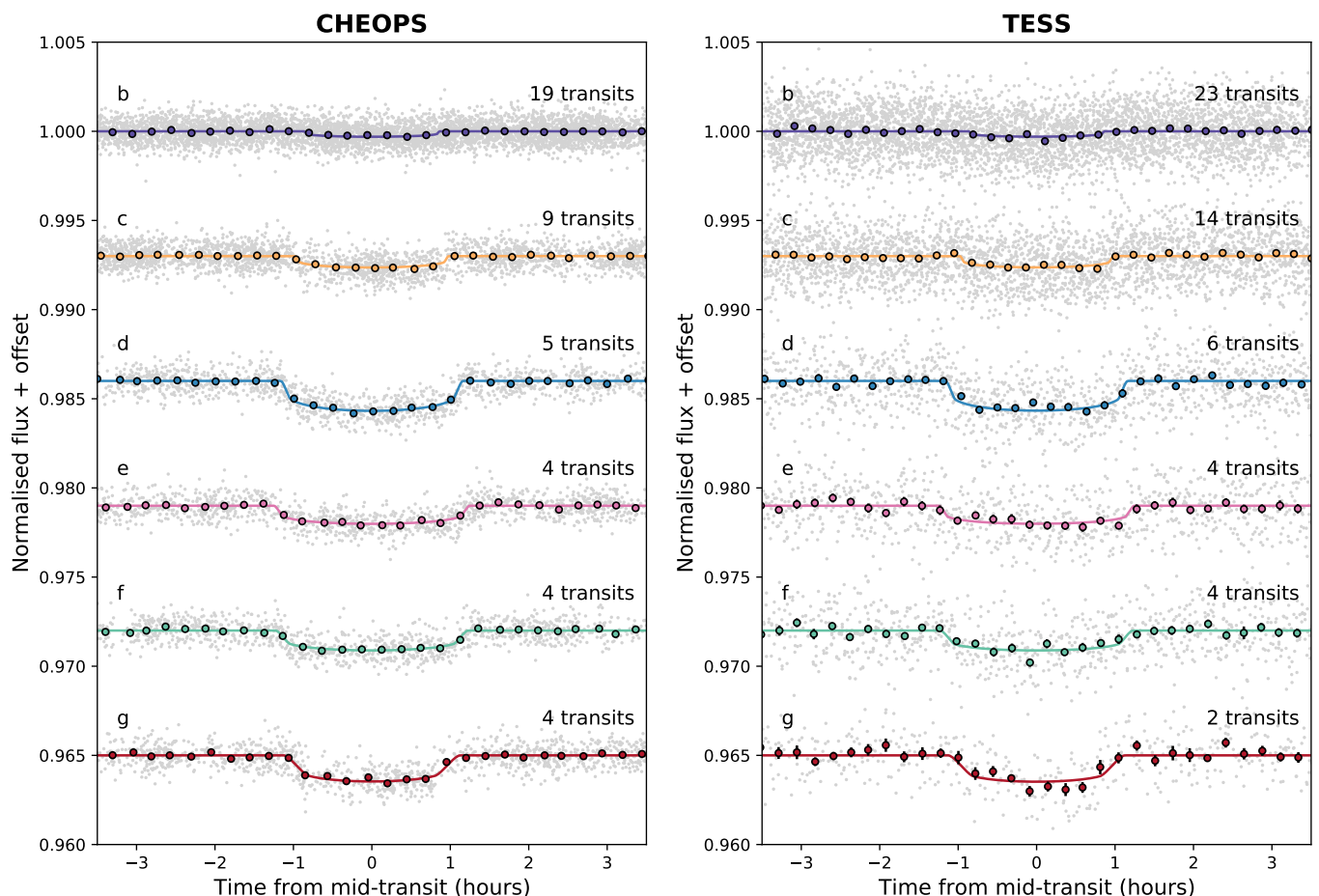


Fig. 1. Phase-folded detrended transit photometry of the TOI-178 planets obtained with CHEOPS (left) and TESS (right). For each planet, the photometry was corrected for the measured TTVs and for the transit signals of the other planets. The unbinned data points are shown in grey, while the coloured circles with error bars correspond to 15-min bins. The coloured lines show the best-fit transit models. The number of transits combined in each phase-folded light curve is also indicated in the plot.

number of light curves, the coefficients of the photometric baseline models were not sampled by the MCMC but determined by a least-squares fit to the residuals at each step of the procedure. This approach allowed us to avoid a dramatic increase in the number of sampled parameters while still fitting the correlated noise simultaneously with the transits (instead of pre-detrending the data), thus ensuring a better propagation of the uncertainties to the derived system parameters of interest (see also similar TTV studies of the TRAPPIST-1 planets by Delrez et al. 2018 and Ducrot et al. 2020).

The prior distributions used in our analysis are summarised in Table B.2. We assumed normal priors for M_* , R_* , and T_{eff} based on the values and uncertainties derived in Sect. 2 (Table 1). We also computed normal priors for the quadratic limb-darkening coefficients (u_1 and u_2) in each bandpass using the LDCU⁵ code (Deline et al. 2022), which builds on the method described by Espinoza & Jordán (2015) to generate limb-darkening coefficients from two libraries of synthetic stellar spectra, ATLAS (Kurucz 1979) and PHOENIX (Husser et al. 2013), while propagating the uncertainties on the stellar parameters and models.

We first ran a preliminary MCMC chain of 50 000 steps to estimate the two scaling factors, β_w and β_r (Table B.1), to be applied to the photometric error bars of each light curve to ac-

count respectively for over- or under-estimated white noise and the presence of residual correlated (red) noise (for details, see Gillon et al. 2012 and references therein). With the corrected photometric error bars, we then ran two chains of 250 000 steps each (including 25% burn-in) and checked their convergence by using the statistical test of Gelman & Rubin (1992), ensuring that the test values for all sampled parameters were <1.01 .

Fig. 1 shows for each planet the phase-folded (TTV-corrected) detrended transit photometry from CHEOPS (left) and TESS (right), with the corresponding best-fit transit models. The medians and $1-\sigma$ credible intervals of the posterior distributions obtained for the system parameters are given in Tables 3 (planets *b*, *c*, and *d*) and 4 (planets *e*, *f*, and *g*). The transit parameters of the six planets are significantly refined compared to L21, most notably their radii, for which we now obtain a relative precision $\lesssim 3\%$ for all planets, except the smallest planet *b* for which the precision is 5.1%. Table C.1 presents the individual transit timings that we obtained for the five outer planets. For each of these planets, we performed a linear fit of these transit timings as a function of their epochs to derive updated mean transit ephemerides, which are also given in Tables 3 and 4. The reduced χ^2 values of these linear fits are 0.8, 0.9, 2.9, 1.4, and 4.3 for TOI-178 *c*, *d*, *e*, *f*, and *g*, respectively. The TTVs with respect to the updated ephemerides are given in Table C.1 and shown in Fig. 2. Only the latest transit of TOI-178 *g* observed with CHEOPS shows a TTV different from zero at the $\sim 3-\sigma$

⁵ <https://github.com/delinea/LDCU>

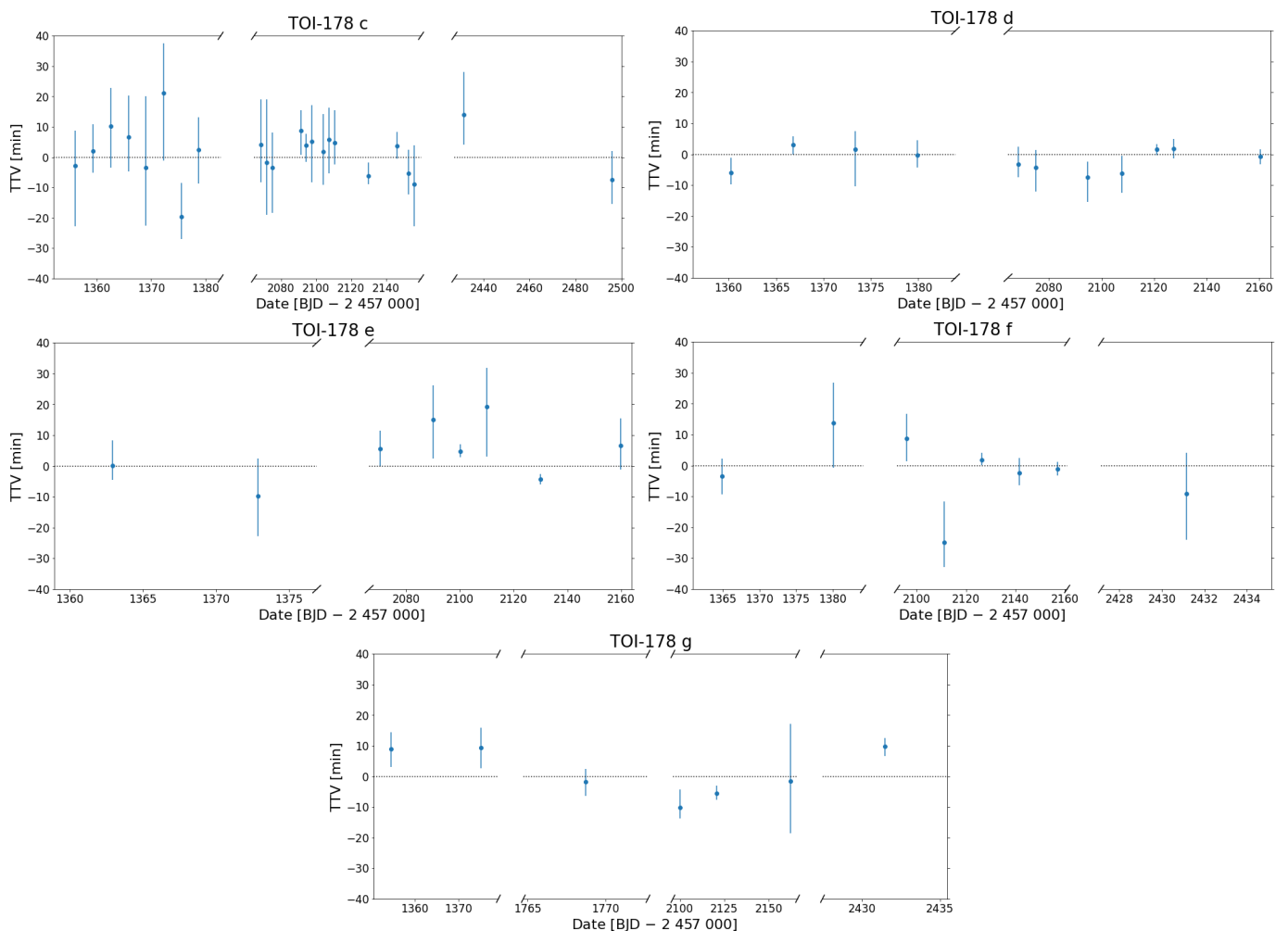


Fig. 2. TTVs (in minutes) deduced from our global transit analysis (see Sect. 4.1) for the five outer TOI-178 planets. These TTVs are relative to the updated mean transit ephemerides given in Tables 3 (planets *b*, *c*, and *d*) and 4 (planets *e*, *f*, and *g*). For each planet, we zoomed around the epochs of the observed transits in the *x*-axes for a better visual assessment of the measured TTVs.

level. A detailed dynamical analysis of the measured transit timings will be presented in Sect. 5.

4.2. Search for additional transiting planets and detection limits

In this section, we first aim to use our large photometric dataset to search for additional transiting planets in the system. We then perform transit injection-and-recovery tests to assess the detection limits of the data and thus place constraints on the radii and orbital periods of potential additional transiting planets in the system.

4.2.1. Search for additional transiting planets

We first searched the TESS data for additional transit signals using the SHERLOCK⁶ pipeline presented in Pozuelos et al. (2020, 2023). SHERLOCK downloads the PDCSAP light curve from MAST and, using the *Wotan* package (Hippke et al. 2019), applies a biweight sliding filter with varying window sizes to detrend the data. The motivation behind this multi-detrend ap-

⁶ The SHERLOCK (Searching for Hints of Exoplanets fRom Lightcurves Of spaCe-based seeKers) code is fully available on GitHub: <https://github.com/franpoz/SHERLOCK>

proach is related to the risk of removing transit signals when detrending the light curve, especially short and shallow ones. Each detrended light curve and the original PDCSAP light curve are then searched for transit signals using the transit least squares (TLS) algorithm (Hippke & Heller 2019). The transit search is carried out in a loop: once a signal is found, it is stored and masked, and then the search keeps running until no more signals above a user-defined signal detection efficiency (SDE, Hippke & Heller 2019) threshold are found in the dataset. Each of these search-find-mask iterations is called a ‘run’. Here, we analysed the 2 TESS sectors simultaneously and tested 10 different window sizes between 0.2 and 1.2 days for the detrending. We searched the PDCSAP and the 10 detrended light curves for periodic signals with orbital periods ranging from 0.5 to 60 days. For each run, we selected the signal which was found in the greatest number of light curves among these 11 light curves, and with the highest SDE. We recovered the 6 known planets in the first 6 runs in the following order: first TOI-178 d, then TOI-178 c, TOI-178 e, TOI-178 f, TOI-178 b, and finally TOI-178 g. In the subsequent runs, we did not find any other promising signal with a $SDE \geq 5$ that could hint at the presence of extra transiting planets in the system.

We then ran SHERLOCK on the CHEOPS data following the same procedure. For this purpose, we pre-detrended the

Parameter (unit)	Leleu et al. (2021)	This work
TOI-178 b		
Transit depth, dF (ppm)	263^{+32}_{-30}	249^{+24}_{-23}
Transit impact parameter, b (R_{\star})	$0.17^{+0.19}_{-0.13}$	$0.25^{+0.15}_{-0.13}$
Orbital period, P (d)	1.914558 ± 0.000018	$1.914554^{+0.000018}_{-0.000015}$
Mid-transit time, T_0 (BJD _{TDB} - 2 450 000)	$8\,741.6365^{+0.0043}_{-0.0030}$	$8\,931.1779^{+0.0023}_{-0.0017}$
Transit duration, W (hours)	$1.692^{+0.056}_{-0.086}$	$1.705^{+0.033}_{-0.076}$
Orbital inclination, i_p (deg)	$88.8^{+0.8}_{-1.3}$	$88.33^{+0.88}_{-1.03}$
Orbital semi-major axis, a_p (au)	0.02607 ± 0.00078	$0.02609^{+0.00031}_{-0.00034}$
Scale parameter, a_p/R_{\star}	$8.61^{+0.21}_{-0.22}$	$8.47^{+0.12}_{-0.13}$
Radius, R_p (R_{\oplus})	$1.152^{+0.073}_{-0.070}$ (6.3%)	1.142 ± 0.058 (5.1%)
Stellar irradiation, S_p (S_{\oplus})	–	198 ± 14
TOI-178 c		
Transit depth, dF (ppm)	551^{+68}_{-59}	542^{+29}_{-24}
Transit impact parameter, b (R_{\star})	$0.34^{+0.30}_{-0.23}$	0.24 ± 0.14
Orbital period, P (d)	$3.238450^{+0.000020}_{-0.000019}$	3.238449 ± 0.000011
Mid-transit time, T_0 (BJD _{TDB} - 2 450 000)	$8\,741.4783^{+0.0034}_{-0.0029}$	$8\,926.0680 \pm 0.0011$
Transit duration, W (hours)	$1.95^{+0.15}_{-0.25}$	$2.045^{+0.047}_{-0.083}$
Orbital inclination, i_p (deg)	$88.4^{+1.1}_{-1.6}$	$88.86^{+0.69}_{-0.70}$
Orbital semi-major axis, a_p (au)	0.0370 ± 0.0011	$0.03703^{+0.00044}_{-0.00048}$
Scale parameter, a_p/R_{\star}	$12.23^{+0.29}_{-0.31}$	$12.03^{+0.18}_{-0.19}$
Radius, R_p (R_{\oplus})	$1.669^{+0.114}_{-0.099}$ (6.8%)	$1.685^{+0.052}_{-0.051}$ (3.1%)
Stellar irradiation, S_p (S_{\oplus})	–	98.3 ± 7.2
Orbital eccentricity (TTVs), e_p	–	$0.0073^{+0.0083}_{-0.0051}$
TOI-178 d		
Transit depth, dF (ppm)	1313^{+64}_{-65}	1414^{+50}_{-51}
Transit impact parameter, b (R_{\star})	$0.485^{+0.051}_{-0.060}$	$0.530^{+0.032}_{-0.035}$
Orbital period, P (d)	6.557700 ± 0.000016	6.557721 ± 0.000013
Mid-transit time, T_0 (BJD _{TDB} - 2 450 000)	$8\,747.14623^{+0.00087}_{-0.00095}$	$8\,760.26373 \pm 0.00074$
Transit duration, W (hours)	$2.346^{+0.047}_{-0.046}$	$2.323^{+0.041}_{-0.034}$
Orbital inclination, i_p (deg)	$88.58^{+0.20}_{-0.18}$	$88.42^{+0.12}_{-0.11}$
Orbital semi-major axis, a_p (au)	0.0592 ± 0.0018	$0.05927^{+0.00070}_{-0.00077}$
Scale parameter, a_p/R_{\star}	$19.57^{+0.47}_{-0.49}$	$19.25^{+0.28}_{-0.30}$
Radius, R_p (R_{\oplus})	$2.572^{+0.075}_{-0.078}$ (3.0%)	$2.717^{+0.066}_{-0.061}$ (2.4%)
Stellar irradiation, S_p (S_{\oplus})	–	38.4 ± 2.8
Orbital eccentricity (TTVs), e_p	–	$0.010^{+0.011}_{-0.007}$

Table 3. Properties of the TOI-178 b, c, and d planets based on our global transit analysis (see Sect. 4.1). For planets *c* and *d*, we also give the eccentricities derived from our TTV analysis (see Sect. 5). For each parameter, we indicate the median of the posterior distribution, along with the 1- σ credible intervals. For the planetary radii, we also give the relative uncertainties in brackets.

CHEOPS photometry using a cubic spline against the spacecraft roll angle to remove most instrumental noise (e.g. Maxted et al. 2022). We performed a transit search on this light curve as well as 10 further-detrended light curves, each obtained by applying a different biweight time-windowed sliding filter to the first light curve. As with the TESS data, we tested 10 window sizes between 0.2 and 1.2 days. We recovered again the 6 known planets in the first 6 runs: first TOI-178 d, then TOI-178 g, TOI-178 e, TOI-178 f, TOI-178 c, and finally TOI-178 b. Unfortunately, the subsequent runs did not reveal any other promising transit signal.

4.2.2. Detection limits

To assess the detection limits of the data, we performed transit injection-and-recovery tests using the MATRIX ToolKit⁷ (Dévora-Pajares & Pozuelos 2022, see also Pozuelos et al. 2020, 2023). We analysed the TESS and CHEOPS data separately, using the same input light curves as for our SHERLOCK transit searches for consistency. For both datasets, we explored plane-

⁷ The MATRIX ToolKit (Multi-phase Transits Recovery from Injected eXoplanets ToolKit) code is available on GitHub: <https://github.com/PlanetHunters/tkmatrix>

Parameter (unit)	Leleu et al. (2021)	This work
TOI-178 e		
Transit depth, dF (ppm)	968^{+69}_{-71}	917^{+33}_{-36}
Transit impact parameter, b (R_\star)	$0.583^{+0.046}_{-0.066}$	$0.595^{+0.024}_{-0.025}$
Orbital period, P (d)	9.961881 ± 0.000042	9.961815 ± 0.000090
Mid-transit time, T_0 (BJD _{TDB} - 2 450 000)	$8\,751.4658^{+0.0016}_{-0.0019}$	$8\,761.4267 \pm 0.0032$
Transit duration, W (hours)	$2.501^{+0.106}_{-0.077}$	$2.517^{+0.045}_{-0.041}$
Orbital inclination, i_p (deg)	$88.71^{+0.16}_{-0.13}$	$88.662^{+0.066}_{-0.071}$
Orbital semi-major axis, a_p (au)	$0.07833^{+0.00093}_{-0.00103}$	$0.02609^{+0.00031}_{-0.00034}$
Scale parameter, a_p/R_\star	$25.87^{+0.62}_{-0.65}$	$25.44^{+0.37}_{-0.40}$
Radius, R_p (R_\oplus)	$2.207^{+0.088}_{-0.090}$ (4.1%)	$2.189^{+0.053}_{-0.058}$ (2.6%)
Stellar irradiation, S_p (S_\oplus)	–	22.0 ± 1.6
Orbital eccentricity (TTVs), e_p	–	$0.0080^{+0.0100}_{-0.0057}$
TOI-178 f		
Transit depth, dF (ppm)	1037^{+94}_{-90}	1154^{+42}_{-53}
Transit impact parameter, b (R_\star)	$0.765^{+0.027}_{-0.031}$	$0.753^{+0.015}_{-0.020}$
Orbital period, P (d)	$15.231915^{+0.000105}_{-0.000095}$	15.231951 ± 0.000095
Mid-transit time, T_0 (BJD _{TDB} - 2 450 000)	$8\,745.7178^{+0.0023}_{-0.0027}$	$8\,898.0349 \pm 0.0017$
Transit duration, W (hours)	$2.348^{+0.097}_{-0.087}$	$2.446^{+0.052}_{-0.043}$
Orbital inclination, i_p (deg)	$88.723^{+0.071}_{-0.069}$	$88.723^{+0.047}_{-0.044}$
Orbital semi-major axis, a_p (au)	0.1039 ± 0.0031	$0.1040^{+0.0012}_{-0.0014}$
Scale parameter, a_p/R_\star	$34.33^{+0.82}_{-0.87}$	$33.76^{+0.49}_{-0.53}$
Radius, R_p (R_\oplus)	$2.287^{+0.108}_{-0.110}$ (4.8%)	$2.455^{+0.061}_{-0.073}$ (3.0%)
Stellar irradiation, S_p (S_\oplus)	–	12.47 ± 0.91
Orbital eccentricity (TTVs), e_p	–	$0.0105^{+0.0071}_{-0.0061}$
TOI-178 g		
Transit depth, dF (ppm)	1633^{+157}_{-139}	1620^{+54}_{-62}
Transit impact parameter, b (R_\star)	$0.866^{+0.017}_{-0.019}$	$0.863^{+0.0097}_{-0.0105}$
Orbital period, P (d)	$20.70950^{+0.00014}_{-0.00011}$	20.70991 ± 0.00015
Mid-transit time, T_0 (BJD _{TDB} - 2 450 000)	$8\,748.0302^{+0.0023}_{-0.0017}$	$8\,893.0016 \pm 0.0026$
Transit duration, W (hours)	$2.167^{+0.090}_{-0.082}$	$2.218^{+0.061}_{-0.058}$
Orbital inclination, i_p (deg)	$88.823^{+0.045}_{-0.047}$	$88.806^{+0.023}_{-0.024}$
Orbital semi-major axis, a_p (au)	$0.1275^{+0.0038}_{-0.0039}$	$0.1276^{+0.0015}_{-0.0017}$
Scale parameter, a_p/R_\star	$42.13^{+1.01}_{-1.06}$	$41.43^{+0.61}_{-0.64}$
Radius, R_p (R_\oplus)	$2.87^{+0.14}_{-0.13}$ (4.9%)	$2.908^{+0.068}_{-0.070}$ (2.4%)
Stellar irradiation, S_p (S_\oplus)	–	$8.28^{+0.60}_{-0.61}$
Orbital eccentricity (TTVs), e_p	–	$0.0056^{+0.0058}_{-0.0039}$

Table 4. Properties of the TOI-178 e, f, and g planets based on our global transit analysis (see Sect. 4.1). We also give the eccentricities derived from our TTV analysis (see Sect. 5). For each parameter, we indicate the median of the posterior distribution, along with the 1- σ credible intervals. For the planetary radii, we also give the relative uncertainties in brackets.

tary radii R_p between 0.5 and 3.5 R_\oplus with steps of 0.2 R_\oplus and orbital periods P between 1 and 30 days with steps of 1 day. For each $R_p - P$ combination, we injected synthetic transits at 12 random phases (i.e. 12 different values for T_0), thus giving a total of 5760 scenarios for each dataset. For simplicity, we assumed the impact parameters and eccentricities of the injected planets were zero. For computational cost reasons, only one detrending can be applied to the resulting light curves before trying to recover the injected transits. We chose here to use a biweight filter with a window size of 0.6 day for TESS and 0.8 day for CHEOPS.

These window sizes were found to give the best results for the known planets during the SHERLOCK searches described above. We also masked the transits of the 6 known planets. During the transit recovery attempts, we considered a synthetic planet to be properly recovered when its epoch was found with 1 hour accuracy and the recovered period was within 5% of the injected period. Finally, it is worth noting that since we injected the synthetic signals into the PDCSAP light curves for TESS and the roll-angle-decorrelated light curves for CHEOPS, our results do not take into account the possible impact of these systematics

corrections on the injected transits. The derived detection limits (discussed below) should therefore be considered rather optimistic (see, e.g., Pozuelo et al. 2020, Eisner et al. 2020).

Fig. 3 shows the two detectability maps in the $R_p - P$ parameter space that we obtained for the TESS (upper panel) and CHEOPS (lower panel) data based on these transit injection-and-recovery tests. We first note that our goal here is not to compare the performances of TESS and CHEOPS. While CHEOPS’s larger primary aperture size and smaller pixel scale make it a higher-precision instrument relative to TESS, the detectability of a transiting planet with a given R_p , P and T_0 will also strongly depend on the number of in-transit data points. In this context, it should be noted that the temporal coverage of the two datasets considered here is very different: the TESS data consist of two sets of nearly-continuous 28-day observations performed in 2018 and 2020, while the CHEOPS data include a nearly-continuous 11-day observation as well as targeted transit windows of the known planets and short observations at random times (fillers, see Sect. 3.1) performed in 2020 and 2021. The CHEOPS data also have a varying observing efficiency depending on the date of observation (see Sect. 3.1). The difference in the number of in-transit data points between the TESS and CHEOPS datasets can thus be very variable depending on the considered scenario. These considerations show that it is necessary to work on a case-by-case basis (i.e. for each $R_p - P - T_0$ scenario) if we want to compare the performances of both instruments (see Oddo et al. 2023 for a detailed discussion on this subject). This is not our goal here, which is rather to get a global picture of the overall detection potential of both datasets in the $R_p - P$ parameter space. In this regard, Fig. 3 shows that additional transiting planets in the system with radii $>1.75 R_\oplus$ and orbital periods <12 days can be reasonably ruled out, as they should have been easily detected (recovery rates $\gtrsim 70\%$ in the TESS data and $\gtrsim 50\%$ in the CHEOPS data). The same planetary sizes but with orbital periods between 12 and 24 days have recovery rates ranging from ~ 70 to 20% . Planets of any size with orbital periods >24 days have recovery rates $<20\%$. Planets with sizes between 1.5 and $1.75 R_\oplus$ have recovery rates $\gtrsim 50\%$ for orbital periods <9 days, while smaller planets with sizes between 1.0 and $1.5 R_\oplus$ only have such reasonably good recovery rates for short orbital periods <3 days. Planets smaller than $1 R_\oplus$ would remain undetected in the current dataset, except maybe for short orbital periods <3 days (recovery rate $\sim 12\%$ in the CHEOPS data, so this would be challenging).

5. Dynamical analysis of the transit timings

All consecutive pairs of planets in the system but the innermost one are close to a first-order MMR where $P_{\text{out}}/P_{\text{in}} \approx (k+1)/k$ with k an integer. As none of the pairs are formally inside the 2-planet MMR, we expect TTVs over the super-period (Lithwick et al. 2012):

$$P_{c,d} \equiv \frac{1}{|(k+1)/P_d - k/P_c|} \quad (1)$$

for planets c and d as an example, and similarly for the other near-resonant pairs. For TOI-178, the super-period is almost the same for all the near-resonant pairs of planets, with $P_{c,d} \approx P_{d,e} \approx P_{e,f} \approx P_{f,g} \approx 260$ days. As a result, a Laplace relation links the successive triplets of planets, leading to a slow evolution of the

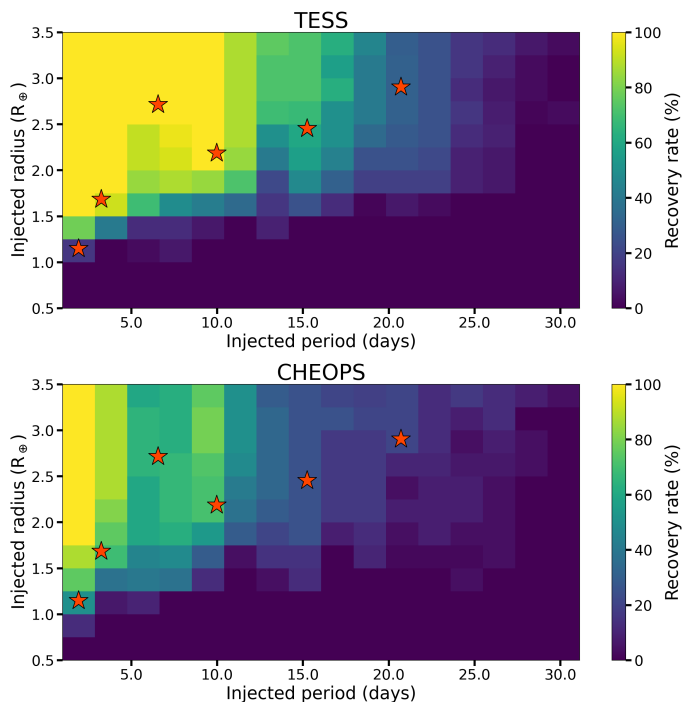


Fig. 3. Results of the transit injection-and-recovery tests performed on the TESS (upper panel) and CHEOPS (lower panel) data to assess the detectability of potential additional transiting planets in the TOI-178 system. For both panels, the red stars show the locations of the 6 known planets in the system.

Laplace angles (see L21):

$$\begin{aligned} \psi_1 &= 1\lambda_c - 4\lambda_d + 3\lambda_e, \\ \psi_2 &= 2\lambda_d - 5\lambda_e + 3\lambda_f, \\ \psi_3 &= 1\lambda_e - 3\lambda_f + 2\lambda_g \end{aligned} \quad (2)$$

where λ_i is the mean longitude of planet i . The evolution of these angles can also produce TTVs on much longer timescales, although according to the mass estimates obtained using radial velocities (see L21), these effects should only start to show with at least 4 years of baseline. Finally, the relative proximity of the planets can also generate a high-frequency chopping signal (Deck & Agol 2015).

We study here the transit timings reported in Table C.1 for the five outer planets. L21 predicted TTV peak-to-peak amplitudes ranging from several minutes for the inner planets to a few tens of minutes for the outer ones. Since the timing uncertainties of the inner planets are comparable to the expected signal, we proceed in two steps. First, we check whether the observed transit timings are consistent with the RV masses and if some constraints on the eccentricities can be obtained by combining the two. As a second step, we then assess the constraints on the masses that can be derived from the TTVs alone.

We fit the TTVs using the code presented in Leleu et al. (2021b): the transit timings are estimated using the TTVfast algorithm (Deck et al. 2014) and the samsam⁸ MCMC algorithm (see Delisle et al. 2018) is used to sample the posteriors. As L21 showed variations in the projected orbital inclination of only about 0.1 degree between the outer planets (Fig. 8 of L21), we

⁸ <https://gitlab.unige.ch/Jean-Baptiste.Delisle/samsam>

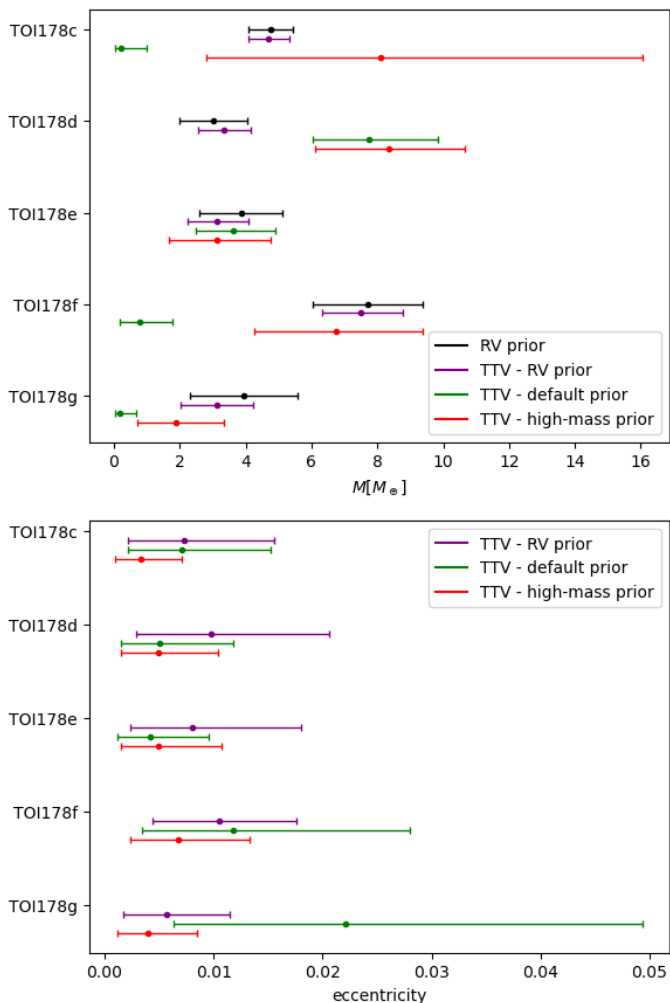


Fig. 4. Mass (upper panel) and eccentricity (lower panel) posteriors derived from our dynamical analysis of the TTVs. The corresponding values are given in Table D.1. In the upper panel, the radial velocity prior based on the RV measurements presented in L21 is shown in black, with 1σ error bars. The coloured error bars show the median and .16-.84 quantiles confidence level of the mass posteriors obtained from our TTV fit using three different sets of priors.

assume in this study that the system is coplanar. The mean longitudes, periods, arguments of periastron, and eccentricities of the planets have uniform priors. For our first test, the mass priors are Gaussian with the respective mean and standard deviation based on the RV posteriors presented in L21. We call this setup the *RV* prior. The mass and eccentricity posteriors of this fit are shown in Fig. 4 and given in Table D.1 (together with the *RV* mass priors for comparison). Fig. 4 shows that, for each planet, the mass posterior of the TTV fit is 1σ consistent with the *RV* prior, implying that the observed TTVs are indeed compatible with the *RV* masses. When using the *RV* mass priors, the TTVs allow us to constrain the eccentricities. L21 set the eccentricities to 0 as the available RVs did not allow a precise measurement, and the stability analysis of the system showed that the eccentricities had to be of a few percent at most. Here, the posteriors of the TTV fit obtained with the *RV* mass priors explore eccentricities that are consistent with both the masses determined from the RVs (all mass posteriors are 1σ consistent with their priors) and the TTV signals. We report the derived eccentricities in Tables 3

(planets *b*, *c*, and *d*) and 4 (planets *e*, *f*, and *g*). The 0.84 quantiles of the eccentricities are below 0.021 for all planets, which is consistent with the stability study of the system presented in L21.

As a second step, we check which constraints on the masses can be obtained from the TTVs alone. The main TTV signal whose period is the aforementioned super-period is degenerate between the planetary masses and eccentricities (Lithwick et al. 2012). The observation of other TTV harmonics, such as the chopping signal or the resonant evolution of the Laplace angle is thus necessary to constrain the planetary masses. Following Hadden & Lithwick (2016, 2017), we hence fit the data with different mass priors to test the robustness of the retrieved masses. The *default* prior is log-uniform in planetary masses, while the *high-mass* prior is uniform in planetary masses. Posteriors that we obtained using these priors are also shown in Fig. 4. We quantify the robustness of the mass determination using the parameter:

$$\Delta_M = \left| \frac{M_{\text{default}}^{.5} - M_{\text{high-mass}}^{.5}}{M_{\text{default}}^{.84} - M_{\text{default}}^{.16}} \right| \quad (3)$$

where $M_{\text{default}}^{.5}$ is the quantile at .5 of the *default* mass posterior, and similarly for other quantities. The robustness mass criterion from Hadden & Lithwick (2017) requires that $\Delta_M < 1$ (note that their criterion is even more conservative as their high-mass prior also contains a log-uniform eccentricity prior, while in our case the eccentricity prior is uniform for all posteriors). The values that we obtained for Δ_M , reported in Table D.1, imply that the mass estimations of planets *c*, *f*, and *g* are highly degenerate ($\Delta_M > 3$ for the three of them). The test finds robust masses for planets *d* and *e*. For TOI-178 *e*, the medians of both the *default* and *high-mass* posteriors are within 1σ of the *RV* prior, while for TOI-178 *d*, the medians of the two posteriors are both outside the 1σ interval of the *RV* prior.

However, the mean log-Likelihood computed for each posterior differs by less than 1 across all three. It implies that the three solutions explain the data equally well and that the various priors explore different parts of the underlying degeneracies. As a result, we recommend keeping for now the *RV* mass estimates presented in L21 as nominal values for the masses of the planets, as we deem the current TTV mass posteriors too much prior-dependent. Nonetheless, the apparent mass shift between the *RV* prior and the higher mass posterior found with both the *default* and *high-mass* priors for TOI-178 *d* highlights the importance of continuing to monitor the system in the future, both in RVs and TTVs. Indeed, TOI-178 *d* had been found by L21 to have a surprisingly low density based on its *RV* mass estimate (Sect. 1). Differences in planet density between *RV*- and *TTV*-characterised systems have been discussed in numerous studies over the last decade (e.g. Hadden & Lithwick 2017; Mills & Mazeh 2017; Leleu et al. 2023). TOI-178 offers the rare opportunity to compare the two techniques for the same system.

Fig. 5 shows the measured transit timings, as well as the TTV posteriors obtained with the *RV* (purple) and *default* (green) mass priors. We note that all current TTV measurements are well explained by the known planets of the system. The TTV signal over the ~ 260 d super-period is clearly visible in the posteriors of all planets. For the *RV* prior, a strong chopping signal is also visible for the two outer planets, while for the *default* prior, the TTVs are explained mainly through the slow evolution of the Laplace angles. A two-year projection after the last observed transit shows that future observations should be able to distinguish between these solutions.

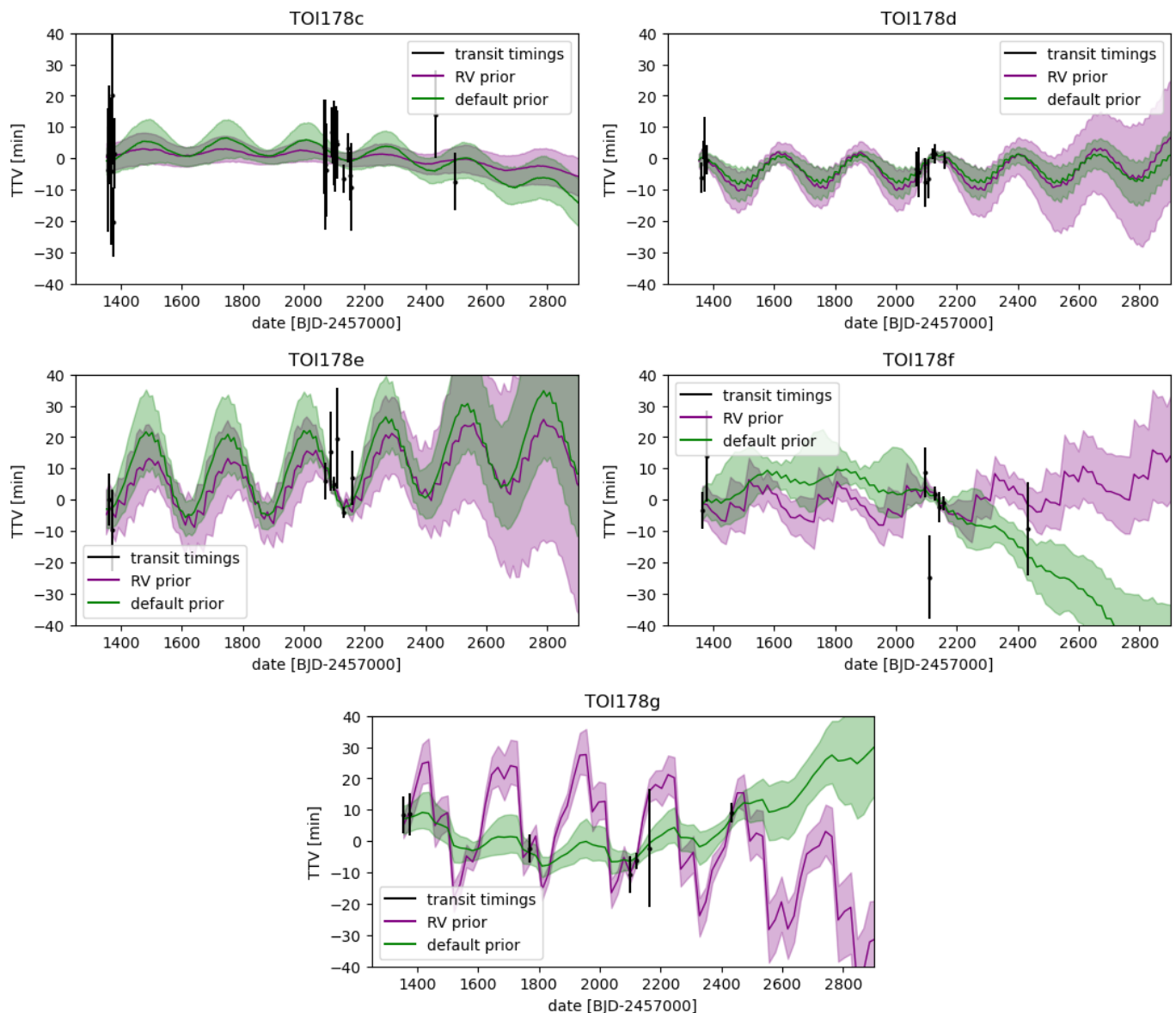


Fig. 5. For each planet, the black points with error bars show the measured TTVs in minutes. For each planet, we also show the median and 1-sigma envelope for the TTVs propagated from 300 randomly-selected samples of the posterior obtained with the *RV* (purple) and *default* (green) mass priors.

Finally, we note that a photodynamical analysis of the light curves, where the gravitational interactions between the planets are taken into account at the stage of the light curve modelling (e.g. [Ragozzine & Holman 2010](#); [Almenara et al. 2018, 2022](#)), could help to better constrain the orbital parameters and masses. In particular, it has been shown that a photodynamical analysis can help to reduce the mass-eccentricity degeneracy when compared to the fit of pre-extracted transit timings, in particular for planets in the super-Earth to mini-Neptune range ([Leleu et al. 2023](#)). Such a photodynamical analysis will be performed in an upcoming paper ([Leleu et al. 2023](#), in prep.).

6. Conclusions

In this work, we presented a detailed photometric study of the TOI-178 system, based on 40 new CHEOPS visits, one new TESS sector, as well as previously published data. We first performed a global analysis of the 100 transits contained in these

data. This enabled us to significantly refine the transit parameters of the six TOI-178 planets, most notably their radii, for which we obtain relative precisions $\lesssim 3\%$, with the exception of the smallest planet *b* for which the precision is 5.1%. We also used our extensive photometric dataset to place constraints on the radii and orbital periods of potential additional transiting planets in the system.

As part of our study, we also performed a first dynamical analysis of the TTVs measured for the five outer planets (*c* to *g*), testing different priors for their masses to assess the robustness of the derived solution. We found that the mass posteriors are very prior-dependent. On one hand, when fitting the TTVs with mass priors based on the previously-published RVs, we find masses that are consistent with the RVs, and eccentricities that are all below 0.02, as expected from stability requirements. On the other hand, when fitting the TTVs with uniform or log-uniform (RV-independent) mass priors, we find mass estimates that are highly degenerate for planets *c*, *f*, and *g*; consistent with the RVs for

planet *e*; and higher than the RV mass for planet *d*. We note that this latter planet had been found by L21 to have a surprisingly low density based on its RV mass estimate. Since the masses derived from the current TTV dataset are very prior-dependent, we recommend keeping for now the RV mass estimates presented in L21 as nominal values for the masses of the planets. Altogether, this first TTV study highlights the importance of continuing to monitor the system in the future, both in RVs and TTVs. In this context, further TTV measurements with CHEOPS and TESS (TOI-178 will be observed again in Sector 69), covering a longer temporal baseline, should help to break the degeneracies and improve our understanding of this benchmark planetary system.

Acknowledgements. CHEOPS is an ESA mission in partnership with Switzerland with important contributions to the payload and the ground segment from Austria, Belgium, France, Germany, Hungary, Italy, Portugal, Spain, Sweden, and the United Kingdom. The CHEOPS Consortium would like to gratefully acknowledge the support received by all the agencies, offices, universities, and industries involved. Their flexibility and willingness to explore new approaches were essential to the success of this mission. The Belgian participation to CHEOPS has been supported by the Belgian Federal Science Policy Office (BELSPO) in the framework of the PRODEX Program, and by the University of Liège through an ARC grant for Concerted Research Actions financed by the Wallonia-Brussels Federation. L.D. is an F.R.S.-FNRS Postdoctoral Researcher. This work has been carried out within the framework of the NCCR PlanetS supported by the Swiss National Science Foundation under grants 51NF40_182901 and 51NF40_205606. A.Br. was supported by the SNSA. M.G. is an F.R.S.-FNRS Senior Research Associate. ACC acknowledges support from STFC consolidated grant numbers ST/R000824/1 and ST/V000861/1, and UKSA grant number ST/R003203/1. This work was also partially supported by a grant from the Simons Foundation (PI Queloz, grant number 327127). V.V.G. is an F.R.S.-FNRS Research Associate. A.C.C. and T.G.W. acknowledge support from STFC consolidated grant numbers ST/R000824/1 and ST/V000861/1, and UKSA grant number ST/R003203/1. Y.A. and M.J.H. acknowledge the support of the Swiss National Fund under grant 200020_172746. We acknowledge support from the Spanish Ministry of Science and Innovation and the European Regional Development Fund through grants ESP2016-80435-C2-1-R, ESP2016-80435-C2-2-R, PGC2018-098153-B-C33, PGC2018-098153-B-C31, ESP2017-87676-C5-1-R, MDM-2017-0737 Unidad de Excelencia Maria de Maeztu-Centro de Astrobiología (INTA-CSIC), as well as the support of the Generalitat de Catalunya/CERCA programme. The MOC activities have been supported by the ESA contract No. 4000124370. S.C.C.B. acknowledges support from FCT through FCT contracts nr. IF/01312/2014/CP1215/CT0004. X.B., S.C., D.G., M.F. and J.L. acknowledge their role as ESA-appointed CHEOPS science team members. L.Bo., G.Br., V.Na., I.Pa., G.Pi., R.Ra., G.Sc., V.Si., and T.Zi. acknowledge support from CHEOPS ASI-INAF agreement n. 2019-29-HH.0. P.E.C. is funded by the Austrian Science Fund (FWF) Erwin Schrödinger Fellowship, program J4595-N. This project was supported by the CNES. This work was supported by FCT - Fundação para a Ciência e a Tecnologia through national funds and by FEDER through COMPETE2020 - Programa Operacional Competitividade e Internacionalização by these grants: UID/FIS/04434/2019, UIDB/04434/2020, UIDP/04434/2020, PTDC/FIS-AST/32113/2017 & POCI-01-0145-FEDER-032113, PTDC/FIS-AST/28953/2017 & POCI-01-0145-FEDER-028953, PTDC/FIS-AST/28987/2017 & POCI-01-0145-FEDER-028987. O.D.S.D. is supported in the form of work contract (DL 57/2016/CP1364/CT0004) funded by national funds through FCT. B.-O.D. acknowledges support from the Swiss State Secretariat for Education, Research and Innovation (SERI) under contract number MB22.00046. This project has received funding from the European Research Council (ERC) under the European Union's Horizon 2020 research and innovation programme (project FOUR ACES, grant agreement No 724427). It has also been carried out in the frame of the National Centre for Competence in Research PlanetS supported by the Swiss National Science Foundation (SNSF). D.E. acknowledges financial support from the Swiss National Science Foundation for project 200021_200726. M.F. gratefully acknowledges the support of the Swedish National Space Agency (DNR 65/19, 174/18). D.G. gratefully acknowledges financial support from the CRT foundation under Grant No. 2018.2323 'Gaseous or rocky? Unveiling the nature of small worlds'. S.H. gratefully acknowledges CNES funding through the grant 837319. K.G.I. is the ESA CHEOPS Project Scientist and is responsible for the ESA CHEOPS Guest Observers Programme. She does not participate in, or contribute to, the definition of the Guaranteed Time Programme of the CHEOPS mission through which observations described in this paper have been taken, nor to any aspect of target selection for the programme. This work was granted access to the HPC resources of MesoPSL financed by the Region Ile de

France and the project Equip@Meso (reference ANR-10-EQPX-29-01) of the programme Investissements d'Avenir supervised by the Agence Nationale pour la Recherche. M.L. acknowledges support of the Swiss National Science Foundation under grant number PCEFP2_194576. R.L. acknowledges funding from University of La Laguna through the Margarita Salas Fellowship from the Spanish Ministry of Universities ref. UNI/551/2021-May 26, and under the EU Next Generation funds. P.M. acknowledges support from STFC research grant number ST/M001040/1. I.Ri. acknowledges support from the Spanish Ministry of Science and Innovation and the European Regional Development Fund through grant PGC2018-098153-B-C33, as well as the support of the Generalitat de Catalunya/CERCA programme. S.G.S. acknowledge support from FCT through FCT contract nr. CEECIND/00826/2018 and POPH/FSE (EC). Gy.M.Sz. acknowledges the support of the Hungarian National Research, Development and Innovation Office (NKFIH) grant K-125015, a PRODEX Experiment Agreement No. 4000137122, the Lendület LP2018-7/2021 grant of the Hungarian Academy of Science and the support of the city of Szombathely. N.A.W. acknowledges UKSA grant ST/R004838/1. Funding for the TESS mission is provided by the NASA's Science Mission Directorate. We acknowledge the use of public TESS data from pipelines at the TESS Science Office and at the TESS Science Processing Operations Center. Resources supporting this work were provided by the NASA High-End Computing (HEC) Program through the NASA Advanced Supercomputing (NAS) Division at Ames Research Center for the production of the SPOC data products. This paper includes data collected by the TESS mission that are publicly available from the Mikulski Archive for Space Telescopes (MAST). We thank the anonymous referee for taking the time to review our work and for her/his valuable suggestions.

References

- Acuña, L., Lopez, T. A., Morel, T., et al. 2022, *A&A*, 660, A102
- Almenara, J. M., Díaz, R. F., Dorn, C., Bonfils, X., & Udry, S. 2018, *MNRAS*, 478, 460
- Almenara, J. M., Hébrard, G., Díaz, R. F., et al. 2022, *A&A*, 663, A134
- Benz, W., Broeg, C., Fortier, A., et al. 2021, *Experimental Astronomy*, 51, 109
- Blackwell, D. E. & Shallis, M. J. 1977, *MNRAS*, 180, 177
- Bonfanti, A., Delrez, L., Hooton, M. J., et al. 2021, *A&A*, 646, A157
- Bonfanti, A., Ortolani, S., & Nascimbeni, V. 2016, *A&A*, 585, A5
- Bonfanti, A., Ortolani, S., Piotto, G., & Nascimbeni, V. 2015, *A&A*, 575, A18
- Brandeker, A., Heng, K., Lendl, M., et al. 2022, *A&A*, 659, L4
- Castelli, F. & Kurucz, R. L. 2003, in *IAU Symposium*, Vol. 210, *Modelling of Stellar Atmospheres*, ed. N. Piskunov, V. W. Weiss, & D. F. Gray, A20
- Christiansen, J. L., Crossfield, I. J. M., Barentsen, G., et al. 2018, *AJ*, 155, 57
- Dai, F., Masuda, K., Beard, C., et al. 2023, *AJ*, 165, 33
- Deck, K. M. & Agol, E. 2015, *ApJ*, 802, 116
- Deck, K. M., Agol, E., Holman, M. J., & Nesvorný, D. 2014, *ApJ*, 787, 132
- Deline, A., Hooton, M. J., Lendl, M., et al. 2022, *A&A*, 659, A74
- Delisle, J. B., Ségransan, D., Dumusque, X., et al. 2018, *A&A*, 614, A133
- Delrez, L., Gillon, M., Triaud, A. H. M. J., et al. 2018, *MNRAS*, 475, 3577
- Dévora-Pajares, M. & Pozuelos, F. J. 2022, *MATRIX: Multi-phAse Transits Recovery from Injected exoplanets*, Zenodo
- Ducrot, E., Gillon, M., Delrez, L., et al. 2020, *A&A*, 640, A112
- Eisner, N. L., Barragán, O., Aigrain, S., et al. 2020, *MNRAS*, 494, 750
- Espinoza, N. & Jordán, A. 2015, *MNRAS*, 450, 1879
- Gaia Collaboration, Brown, A. G. A., Vallenari, A., et al. 2018, *A&A*, 616, A1
- Gaia Collaboration, Brown, A. G. A., Vallenari, A., et al. 2021, *A&A*, 649, A1
- Gelman, A. & Rubin, D. B. 1992, *Statistical Science*, 7, 457
- Gillon, M., Demory, B. O., Madhusudhan, N., et al. 2014, *A&A*, 563, A21
- Gillon, M., Triaud, A. H. M. J., Demory, B.-O., et al. 2017, *Nature*, 542, 456
- Gillon, M., Triaud, A. H. M. J., Fortney, J. J., et al. 2012, *A&A*, 542, A4
- Goździewski, K., Migaszewski, C., Panichi, F., & Szuszkiewicz, E. 2016, *MNRAS*, 455, L104
- Hadden, S. & Lithwick, Y. 2016, *ApJ*, 828, 44
- Hadden, S. & Lithwick, Y. 2017, *AJ*, 154, 5
- Hippke, M., David, T. J., Mulders, G. D., & Heller, R. 2019, *AJ*, 158, 143
- Hippke, M. & Heller, R. 2019, *A&A*, 623, A39
- Hoyer, S., Guterman, P., Demangeon, O., et al. 2020, *A&A*, 635, A24
- Husser, T. O., Wende-von Berg, S., Dreizler, S., et al. 2013, *A&A*, 553, A6
- Jenkins, J. M., Twicken, J. D., McCauliff, S., et al. 2016, in *Society of Photo-Optical Instrumentation Engineers (SPIE) Conference Series*, Vol. 9913, *Software and Cyberinfrastructure for Astronomy IV*, ed. G. Chiozzi & J. C. Zuzman, 99133E
- Kipping, D. M. 2013, *MNRAS*, 435, 2152
- Kurucz, R. L. 1979, *ApJS*, 40, 1
- Leleu, A., Alibert, Y., Hara, N. C., et al. 2021a, *A&A*, 649, A26
- Leleu, A., Chatel, G., Udry, S., et al. 2021b, *A&A*, 655, A66
- Leleu, A., Delisle, J. B., Udry, S., et al. 2023, *A&A*, 669, A117
- Leleu, A., Lillo-Box, J., Sestovic, M., et al. 2019, *A&A*, 624, A46
- Lendl, M., Csizmadia, S., Deline, A., et al. 2020, *A&A*, 643, A94

- Lindgren, L., Bastian, U., Biermann, M., et al. 2021, *A&A*, 649, A4
- Lithwick, Y., Xie, J., & Wu, Y. 2012, *ApJ*, 761, 122
- Lopez, T. A., Barros, S. C. C., Santerne, A., et al. 2019, *A&A*, 631, A90
- Luger, R., Sestovic, M., Kruse, E., et al. 2017, *Nature Astronomy*, 1, 0129
- MacDonald, M. G., Ragozzine, D., Fabrycky, D. C., et al. 2016, *AJ*, 152, 105
- Mandel, K. & Agol, E. 2002, *ApJ*, 580, L171
- Marigo, P., Girardi, L., Bressan, A., et al. 2017, *ApJ*, 835, 77
- Maxted, P. F. L., Ehrenreich, D., Wilson, T. G., et al. 2022, *MNRAS*, 514, 77
- Mills, S. M., Fabrycky, D. C., Migaszewski, C., et al. 2016, *Nature*, 533, 509
- Mills, S. M. & Mazeh, T. 2017, *ApJ*, 839, L8
- Morris, B. M., Heng, K., Brandeker, A., Swan, A., & Lendl, M. 2021, *A&A*, 651, L12
- Oddo, D., Dragomir, D., Brandeker, A., et al. 2023, *AJ*, 165, 134
- Pepe, F., Cristiani, S., Rebolo, R., et al. 2021, *A&A*, 645, A96
- Pozuelos, F. J., Suárez, J. C., de Elía, G. C., et al. 2020, *A&A*, 641, A23
- Pozuelos, F. J., Timmermans, M., Rackham, B. V., et al. 2023, *A&A*, 672, A70
- Ragozzine, D. & Holman, M. J. 2010, arXiv e-prints, arXiv:1006.3727
- Ricker, G. R., Winn, J. N., Vanderspek, R., et al. 2015, *Journal of Astronomical Telescopes, Instruments, and Systems*, 1, 014003
- Rivera, E. J., Laughlin, G., Butler, R. P., et al. 2010, *ApJ*, 719, 890
- Salmon, S. J. A. J., Van Grootel, V., Buldgen, G., Dupret, M. A., & Eggenberger, P. 2021, *A&A*, 646, A7
- Schanche, N., Hébrard, G., Collier Cameron, A., et al. 2020, *MNRAS*, 499, 428
- Schwarz, G. 1978, *Annals of Statistics*, 6, 461
- Scuflaire, R., Théado, S., Montalbán, J., et al. 2008, *Ap&SS*, 316, 83
- Skrutskie, M. F., Cutri, R. M., Stiening, R., et al. 2006, *AJ*, 131, 1163
- Smith, J. C., Stumpe, M. C., Van Cleve, J. E., et al. 2012, *PASP*, 124, 1000
- Stumpe, M. C., Smith, J. C., Catanzarite, J. H., et al. 2014, *PASP*, 126, 100
- Stumpe, M. C., Smith, J. C., Van Cleve, J. E., et al. 2012, *PASP*, 124, 985
- Szabó, G. M., Gandolfi, D., Brandeker, A., et al. 2021, *A&A*, 654, A159
- Wheatley, P. J., West, R. G., Goad, M. R., et al. 2018, *MNRAS*, 475, 4476
- Wright, E. L., Eisenhardt, P. R. M., Mainzer, A. K., et al. 2010, *AJ*, 140, 1868
- 21 INAF, Osservatorio Astronomico di Padova, Vicolo dell'Osservatorio 5, 35122 Padova, Italy
- 22 Institute of Optical Sensor Systems, German Aerospace Center (DLR), Rutherfordstrasse 2, 12489 Berlin, Germany
- 23 Institute of Planetary Research, German Aerospace Center (DLR), Rutherfordstrasse 2, 12489 Berlin, Germany
- 24 Université de Paris, Institut de physique du globe de Paris, CNRS, F-75005 Paris, France
- 25 INAF, Osservatorio Astrofisico di Torino, Via Osservatorio, 20, I-10025 Pino Torinese To, Italy
- 26 Centre for Mathematical Sciences, Lund University, Box 118, 221 00 Lund, Sweden
- 27 Aix Marseille Univ, CNRS, CNES, LAM, 38 rue Frédéric Joliot-Curie, 13388 Marseille, France
- 28 Centre Vie dans l'Univers, Faculté des sciences, Université de Genève, Quai Ernest-Ansermet 30, CH-1211 Genève 4, Switzerland
- 29 Leiden Observatory, University of Leiden, PO Box 9513, 2300 RA Leiden, The Netherlands
- 30 Department of Space, Earth and Environment, Chalmers University of Technology, Onsala Space Observatory, 439 92 Onsala, Sweden
- 31 Dipartimento di Fisica, Università degli Studi di Torino, via Pietro Giuria 1, I-10125, Torino, Italy
- 32 University of Vienna, Department of Astrophysics, Türkenschanzstrasse 17, 1180 Vienna, Austria
- 33 Science and Operations Department - Science Division (SCI-SC), Directorate of Science, European Space Agency (ESA), European Space Research and Technology Centre (ESTEC), Keplerlaan 1, 2201-AZ Noordwijk, The Netherlands
- 34 NASA Ames Research Center, Moffett Field, CA 94035, USA
- 35 Konkoly Observatory, Research Centre for Astronomy and Earth Sciences, 1121 Budapest, Konkoly Thege Miklós út 15-17, Hungary
- 36 ELTE Eötvös Loránd University, Institute of Physics, Pázmány Péter sétány 1/A, 1117 Budapest, Hungary
- 37 IMCCE, UMR8028 CNRS, Observatoire de Paris, PSL Univ., Sorbonne Univ., 77 av. Denfert-Rochereau, 75014 Paris, France
- 38 Center for Astrophysics | Harvard & Smithsonian, 60 Garden Street, Cambridge, MA, 02138, USA
- 39 Institut d'astrophysique de Paris, UMR7095 CNRS, Université Pierre & Marie Curie, 98bis blvd. Arago, 75014 Paris, France
- 40 Department of Astronomy and Astrophysics, University of Chicago, Chicago, IL 60637, USA
- 41 Astrophysics Group, Keele University, Staffordshire, ST5 5BG, United Kingdom
- 42 Department of Astrophysics, University of Vienna, Tuerkenschanzstrasse 17, 1180 Vienna, Austria
- 43 INAF, Osservatorio Astrofisico di Catania, Via S. Sofia 78, 95123 Catania, Italy
- 44 Dipartimento di Fisica e Astronomia "Galileo Galilei", Università degli Studi di Padova, Vicolo dell'Osservatorio 3, 35122 Padova, Italy
- 45 Department of Physics, University of Warwick, Gibbet Hill Road, Coventry CV4 7AL, United Kingdom
- 46 Zentrum für Astronomie und Astrophysik, Technische Universität Berlin, Hardenbergstr. 36, D-10623 Berlin, Germany
- 47 Institut für Geologische Wissenschaften, Freie Universität Berlin, 12249 Berlin, Germany
- 48 Kavli Institute for Astrophysics and Space Research, Massachusetts Institute of Technology, Cambridge, MA 02139, USA
- 49 Department of Physics, Massachusetts Institute of Technology, Cambridge, MA 02139, USA
- 50 Department of Earth, Atmospheric and Planetary Science, Massachusetts Institute of Technology, 77 Massachusetts Avenue, Cambridge, MA 02139, USA
- 51 Department of Aeronautics and Astronautics, MIT, 77 Massachusetts Avenue, Cambridge, MA 02139, USA
- 52 ELTE Eötvös Loránd University, Gothard Astrophysical Observatory, 9700 Szombathely, Szent Imre h. u. 112, Hungary
- 53 MTA-ELTE Exoplanet Research Group, 9700 Szombathely, Szent Imre h. u. 112, Hungary
-
- 1 Astrobiology Research Unit, Université de Liège, Allée du 6 Août 19C, B-4000 Liège, Belgium
- 2 Space sciences, Technologies and Astrophysics Research (STAR) Institute, Université de Liège, Allée du 6 Août 19C, 4000 Liège, Belgium
- 3 Observatoire Astronomique de l'Université de Genève, Chemin Pegasi 51, CH-1290 Versoix, Switzerland
- 4 Physikalisches Institut, University of Bern, Sidlerstrasse 5, 3012 Bern, Switzerland
- 5 Department of Astronomy, Stockholm University, AlbaNova University Center, 10691 Stockholm, Sweden
- 6 Cavendish Laboratory, JJ Thomson Avenue, Cambridge CB3 0HE, UK
- 7 Centre for Exoplanet Science, SUPA School of Physics and Astronomy, University of St Andrews, North Haugh, St Andrews KY16 9SS, UK
- 8 Center for Space and Habitability, University of Bern, Gesellschaftsstrasse 6, 3012 Bern, Switzerland
- 9 ETH Zurich, Department of Physics, Wolfgang-Pauli-Strasse 2, CH-8093 Zurich, Switzerland
- 10 Space Research Institute, Austrian Academy of Sciences, Schmiedlstrasse 6, A-8042 Graz, Austria
- 11 Instituto de Astrofísica de Canarias, 38200 La Laguna, Tenerife, Spain
- 12 Departamento de Astrofísica, Universidad de La Laguna, 38206 La Laguna, Tenerife, Spain
- 13 Institut de Ciències de l'Espai (ICE, CSIC), Campus UAB, Can Magrans s/n, 08193 Bellaterra, Spain
- 14 Institut d'Estudis Espacials de Catalunya (IEEC), 08034 Barcelona, Spain
- 15 ESTEC, European Space Agency, 2201AZ, Noordwijk, NL
- 16 Admatis, 5. Kandó Kálmán Street, 3534 Miskolc, Hungary
- 17 Depto. de Astrofísica, Centro de Astrobiología (CSIC-INTA), ESAC campus, 28692 Villanueva de la Cañada (Madrid), Spain
- 18 Instituto de Astrofísica e Ciências do Espaço, Universidade do Porto, CAUP, Rua das Estrelas, 4150-762 Porto, Portugal
- 19 Departamento de Física e Astronomia, Faculdade de Ciências, Universidade do Porto, Rua do Campo Alegre, 4169-007 Porto, Portugal
- 20 Université Grenoble Alpes, CNRS, IPAG, 38000 Grenoble, France

⁵⁴ Institute of Astronomy, University of Cambridge, Madingley Road,
Cambridge, CB3 0HA, United Kingdom

⁵⁵ Department of Astrophysical Sciences, Princeton University, 4 Ivy
Lane, Princeton, NJ 08544, USA

Appendix A: Data: CHEOPS visits

Table A.1. Log of the CHEOPS observations. The file key (first column) is a unique identifier that can be used to retrieve the data from the CHEOPS archive. The efficiency (sixth column) represents the ratio between the amount of science observing time in a visit (excluding the interruptions due to Earth occultations or SAA crossings) and the total duration of the visit (including interruptions). The last two columns give the median absolute deviation (MAD) of the difference between two consecutive data points of the light curve for the CHEOPS Data Reduction Pipeline (DRP) and the PSF photometry pipeline (PIPE).

File key	UTC start	UTC end	Content	N_{frames}	Efficiency (%)	DRP MAD (ppm)	PIPE MAD (ppm)
PR100031_TG028901	2020-07-21 11:01	2020-07-21 14:28	Filler	112	54.1	632	485
PR100031_TG029001	2020-07-25 01:59	2020-07-25 05:13	Filler	109	56.2	598	550
PR100031_TG030201 ^(a)	2020-08-04 22:10	2020-08-09 01:57	b (×2), c, d, e	3253	54.3	662	590
PR100031_TG030301 ^(a)	2020-08-09 02:47	2020-08-15 22:50	b (×4), c (×2), d	5590	56.8	665	590
PR100031_TG030701 ^(a)	2020-09-07 08:06	2020-09-07 21:27	e, g	559	69.7	740	638
PR100031_TG032101	2020-09-20 21:02	2020-09-21 01:54	Filler	257	87.7	741	596
PR100031_TG031001	2020-09-22 21:02	2020-09-23 00:15	Filler	165	85.0	648	583
PR100031_TG031801	2020-09-23 00:26	2020-09-23 05:18	Filler	283	96.5	747	532
PR100031_TG032201	2020-09-28 03:51	2020-09-28 12:17	b, d, g	441	86.9	759	657
PR100031_TG031101	2020-09-29 06:23	2020-09-29 11:24	Filler	253	83.7	631	638
PR100031_TG031201	2020-10-01 07:32	2020-10-01 10:45	Filler	160	82.4	1016	650
PR100031_TG031401	2020-10-03 10:24	2020-10-03 13:37	Filler	180	92.7	879	664
PR100031_TG033301 ^(a)	2020-10-03 18:51	2020-10-04 02:51	b, f	424	88.1	750	593
PR100031_TG031301	2020-10-04 17:02	2020-10-04 19:59	Filler	161	90.4	798	583
PR100031_TG033001	2020-10-04 20:26	2020-10-05 05:09	d	480	91.6	686	550
PR100031_TG033302	2020-10-05 16:42	2020-10-05 23:56	b	379	87.1	825	574
PR100031_TG033101	2020-10-07 06:05	2020-10-07 15:26	c, e	497	88.4	762	604
PR100031_TG033303	2020-10-07 15:37	2020-10-07 22:51	b	372	85.5	844	613
PR100031_TG031901	2020-10-08 22:04	2020-10-09 02:56	Filler	273	93.1	687	602
PR100031_TG032001	2020-10-09 08:10	2020-10-09 13:02	Filler	254	86.6	737	571
PR100031_TG033304	2020-10-09 13:13	2020-10-09 20:20	b	399	93.2	755	593
PR100031_TG033901	2020-10-12 18:09	2020-10-12 23:27	Filler	236	73.9	782	609
PR100031_TG035101	2020-10-19 02:36	2020-10-19 10:20	b, f	333	71.6	734	617
PR100031_TG033902	2020-10-20 00:21	2020-10-20 05:13	Filler	218	74.4	927	633
PR100031_TG034001	2020-10-21 11:19	2020-10-21 14:32	Filler	131	67.5	657	464
PR100031_TG033903	2020-10-22 11:52	2020-10-22 16:41	Filler	193	66.5	796	605
PR100031_TG034201	2020-10-23 15:18	2020-10-23 22:52	c	262	57.6	759	669
PR100031_TG034002	2020-10-24 20:59	2020-10-24 23:52	Filler	97	55.7	892	593
PR100031_TG033904	2020-10-26 06:00	2020-10-26 10:53	Filler	174	59.4	595	469
PR100031_TG034003	2020-10-28 01:30	2020-10-28 04:43	Filler	115	59.3	756	593
PR100031_TG035601	2020-10-28 17:17	2020-10-29 00:16	b	115	59.3	841	736
PR100031_TG033905	2020-10-29 20:30	2020-10-30 01:33	Filler	153	50.3	712	581
PR100031_TG035701	2020-10-30 02:16	2020-10-30 09:46	c	285	63.2	723	647
PR100031_TG035702	2020-11-02 08:03	2020-11-02 16:07	c	274	56.5	715	634
PR100031_TG036101	2020-11-03 07:32	2020-11-03 14:19	b, f	234	57.3	627	614
PR100031_TG036401	2020-11-06 04:41	2020-11-06 14:02	e	289	51.4	644	517
PR100031_TG036301	2020-11-06 14:13	2020-11-06 22:56	d	240	45.8	675	558
PR100031_TG035602	2020-11-07 07:09	2020-11-07 13:55	b	234	57.5	714	626
PR100031_TG036201	2020-11-08 14:11	2020-11-08 22:13	g	218	45.1	766	577
PR100031_TG043601	2021-08-04 09:14	2021-08-04 18:48	b, c, f	306	53.2	691	618
PR100031_TG043701	2021-08-04 19:00	2021-08-05 05:53	c, g	360	55.0	740	668
PR100031_TG043201	2021-10-08 06:52	2021-10-08 14:01	b, c	378	87.9	682	602
PR100031_TG043202	2021-10-15 22:47	2021-10-16 05:56	b	343	79.7	650	552
PR100031_TG043203	2021-10-17 21:29	2021-10-18 04:38	b	304	70.7	679	587

Notes. ^(a) Data previously presented in L21.

Appendix B: Global transit analysis: supplementary material*Appendix B.1: Photometric baseline models and error scaling factors*

Date (UT)	Facility	Planet(s)	Epoch(s)	N_{points}	T_{exp} (s)	Baseline model	Residual RMS (%)	β_w	β_r
2018-09-23	TESS	g	-26	265	120	o	0.118	0.94	1.74
2018-08-24	TESS	b	-301	196	120	o	0.118	0.94	1.29
2018-08-26	TESS	c	-176	218	120	o	0.121	0.96	1.23
2018-08-26	TESS	b	-300	195	120	$p(t)$	0.116	0.92	1.14
2018-08-28	TESS	b	-299	187	120	o	0.123	0.97	1.48
2018-08-28	TESS	c	-175	228	120	o	0.126	1.00	1.08
2018-08-29	TESS	d	-61	247	120	$p(t)$	0.127	1.01	1.08
2018-08-30	TESS	b	-298	197	120	o	0.108	0.86	1.00
2018-08-31	TESS	b, c	-297, -174	229	120	o	0.119	0.94	1.15
2018-09-01	TESS	e	-40	293	120	o	0.114	0.90	1.09
2018-09-02	TESS	b	-296	195	120	o	0.118	0.93	1.00
2018-09-03	TESS	f	-35	283	120	o	0.125	0.97	1.13
2018-09-04	TESS	c	-173	227	120	o	0.118	0.92	1.35
2018-09-04	TESS	b	-295	193	120	o	0.135	1.05	1.28
2018-09-05	TESS	d	-60	235	120	o	0.108	0.84	1.07
2018-09-07	TESS	c	-172	229	120	o	0.133	1.05	1.65
2018-09-08	TESS	b	-293	202	120	o	0.118	0.94	1.33
2018-09-10	TESS	b	-292	196	120	o	0.129	1.02	1.36
2018-09-10	TESS	c	-171	225	120	o	0.119	0.94	1.33
2018-09-11	TESS	e	-39	296	120	o	0.126	1.00	1.79
2018-09-11	TESS	d	-59	239	120	o	0.120	0.95	1.47
2018-09-12	TESS	b	-291	190	120	o	0.111	0.88	1.71
2018-09-13	TESS	g	-25	265	120	o	0.122	0.97	1.65
2018-09-13	TESS	c	-170	226	120	o	0.122	0.97	1.00
2018-09-14	TESS	b	-290	186	120	o	0.111	0.88	1.47
2018-09-16	TESS	b	-289	186	120	o	0.132	1.04	1.59
2018-09-17	TESS	c	-169	206	120	o	0.117	0.92	1.65
2018-09-18	TESS	b	-288	195	120	o	0.121	0.94	1.20
2018-09-18	TESS	d	-58	173	120	o	0.129	1.00	1.02
2018-09-18	TESS	f	-34	268	120	o	0.130	1.00	1.11
2019-09-11	NGTS1	b	-101	2321	10	$p(a)$	0.639	0.72	1.13
2019-09-11	NGTS2	b	-101	2332	10	$p(a)$	0.627	0.75	1.23
2019-09-11	NGTS3	b	-101	2326	10	$p(a)$	0.634	0.76	1.48
2019-09-11	NGTS4	b	-101	2325	10	$p(a)$	0.633	0.74	1.01
2019-09-11	NGTS5	b	-101	2330	10	$p(a)$	0.637	0.75	1.46
2019-09-11	NGTS6	b	-101	2309	10	$p(a)$	0.639	0.78	1.96
2019-10-12	NGTS1	g	-6	1835	10	$p(a)$	0.578	0.60	2.74
2019-10-12	NGTS2	g	-6	1828	10	$p(a)$	0.581	0.60	1.46
2019-10-12	NGTS3	g	-6	1838	10	$p(a)$	0.616	0.61	1.11
2019-10-12	NGTS4	g	-6	1823	10	$p(a)$	0.553	0.56	1.42
2019-10-12	NGTS5	g	-6	1836	10	$p(a)$	0.574	0.60	1.00
2019-10-12	NGTS6	g	-6	1849	10	$p(a)$	0.567	0.59	2.23
2019-10-12	NGTS7	g	-6	1831	10	$p(a)$	0.578	0.59	1.65
2020-08-05	CHEOPS	b	71	206	60	$sp(r) + o$	0.057	1.01	1.28
2020-08-06	CHEOPS	c, d	44, 47	404	60	$sp(r) + o$	0.057	1.00	2.49
2020-08-07	CHEOPS	b	72	190	60	$sp(r) + o$	0.057	1.00	1.55
2020-08-08	CHEOPS	e	31	331	60	$sp(r) + o$	0.057	1.00	2.11
2020-08-09	CHEOPS	b	73	196	60	$sp(r) + o$	0.060	1.07	1.83
2020-08-10	CHEOPS	c	45	185	60	$sp(r) + o$	0.056	1.00	1.07
2020-08-11	CHEOPS	b	74	187	60	$sp(r) + o$	0.056	1.00	1.92
2020-08-12	CHEOPS	b	75	275	60	$sp(r) + o$	0.056	1.01	2.23
2020-08-13	CHEOPS	c, d	46, 48	374	60	$sp(r) + p(b)$	0.058	1.04	2.14
2020-08-15	CHEOPS	b	76	279	60	$sp(r) + o$	0.056	1.00	1.13
2020-08-28	TESS	b, e	83, 33	368	120	o	0.124	0.99	1.19
2020-08-29	TESS	c	51	241	120	o	0.124	0.99	1.00
2020-08-30	TESS	b	84	207	120	o	0.119	0.94	1.09
2020-09-01	TESS	b	85	208	120	o	0.122	0.97	1.26

Continued on next page

Table B.1 – *continued from previous page*

Date (UT)	Facility	Planet(s)	Epoch(s)	N_{points}	T_{exp} (s)	Baseline model	Residual RMS (%)	β_w	β_r
2020-09-01	TESS	c	52	240	120	o	0.115	0.91	1.00
2020-09-02	TESS	d	51	236	120	o	0.131	1.04	1.08
2020-09-03	TESS	b	86	208	120	o	0.110	0.87	1.07
2020-09-03	TESS	f	13	288	120	o	0.112	0.88	1.32
2020-09-04	TESS	b, c	87, 53	361	120	o	0.120	0.93	1.50
2020-09-07	CHEOPS	e, g	34, 10	555	60	$\text{sp}(r) + \text{p}(t)$	0.060	1.06	1.71
2020-09-10	TESS	b	90	207	120	o	0.131	1.03	1.48
2020-09-11	TESS	c	55	238	120	o	0.124	0.98	1.56
2020-09-12	TESS	b	91	207	120	o	0.115	0.91	1.25
2020-09-14	TESS	b	92	195	120	o	0.120	0.95	1.34
2020-09-14	TESS	c	56	216	120	o	0.126	0.99	1.26
2020-09-15	TESS	d	53	287	120	o	0.138	1.09	1.24
2020-09-16	TESS	b	93	207	120	o	0.135	1.07	1.33
2020-09-17	TESS	e	35	308	120	o	0.129	1.02	1.03
2020-09-18	TESS	c	57	240	120	o	0.122	0.96	1.00
2020-09-18	TESS	b	94	207	120	o	0.116	0.91	1.48
2020-09-18	TESS	f	14	267	120	o	0.125	0.98	1.37
2020-09-28	CHEOPS	b, d, g	99, 55, 11	434	60	$\text{sp}(r) + \text{p}(b)$	0.061	1.05	1.16
2020-10-03	CHEOPS	b, f	102, 15	426	60	$\text{sp}(r) + \text{p}(y)$	0.057	1.02	1.25
2020-10-04	CHEOPS	d	56	483	60	$\text{sp}(r) + \text{p}(b)$	0.059	1.05	2.19
2020-10-05	CHEOPS	b	103	365	60	$\text{sp}(r) + \text{p}(b)$	0.057	1.01	1.31
2020-10-07	CHEOPS	c, e	63, 37	486	60	$\text{sp}(r) + \text{p}(y)$	0.059	1.05	1.27
2020-10-07	CHEOPS	b	104	374	60	$\text{sp}(r) + o$	0.056	1.00	1.58
2020-10-09	CHEOPS	b	105	394	60	$\text{sp}(r) + o$	0.058	1.04	1.03
2020-10-19	CHEOPS	b, f	110, 16	329	60	$\text{sp}(r) + \text{p}(t)$	0.057	1.02	1.27
2020-10-23	CHEOPS	c	68	258	60	$\text{sp}(r) + \text{p}(t)$	0.061	1.08	1.16
2020-10-28	CHEOPS	b	115	205	60	$\text{sp}(r) + o$	0.062	1.11	1.36
2020-10-30	CHEOPS	c	70	282	60	$\text{sp}(r) + \text{p}(ttt)$	0.060	1.07	1.68
2020-11-02	CHEOPS	c	71	268	60	$\text{sp}(r) + \text{p}(t)$	0.061	1.09	1.75
2020-11-03	CHEOPS	b, f	118, 17	233	60	$\text{sp}(r) + \text{p}(ttt)$	0.057	1.00	1.49
2020-11-06	CHEOPS	e	40	297	60	$\text{sp}(r) + o$	0.056	1.00	1.84
2020-11-06	CHEOPS	d	61	247	60	$\text{sp}(r) + o$	0.059	1.06	1.90
2020-11-07	CHEOPS	b	120	229	60	$\text{sp}(r) + o$	0.060	1.08	1.41
2020-11-08	CHEOPS	g	13	223	60	$\text{sp}(r) + o$	0.056	1.00	2.56
2021-08-04	CHEOPS	b, f, c	261, 35, 156	293	60	$\text{sp}(r) + o$	0.063	1.12	2.10
2021-08-04	CHEOPS	c, g	156, 26	343	60	$\text{sp}(r) + \text{p}(y)$	0.066	1.18	1.48
2021-10-08	CHEOPS	b, c	295, 176	365	60	$\text{sp}(r) + o$	0.057	1.01	2.66
2021-10-15	CHEOPS	b	299	327	60	$\text{sp}(r) + o$	0.058	1.01	1.47
2021-10-17	CHEOPS	b	300	296	60	$\text{sp}(r) + o$	0.067	1.15	1.43

Table B.1. Photometric baseline models, residual RMS, and error scaling factors β_w and β_r for each transit light curve used in our global transit analysis (see Sect. 4.1). For the baseline function, o is a simple constant (to account for any out-of-transit flux offset), $\text{sp}(r)$ is a cubic spline against the spacecraft roll angle r , and $\text{p}(\alpha)$ denotes a first-order polynomial function of the parameter α , with α that can be $t = \text{time}$, $b = \text{background}$, $a = \text{airmass}$, x and $y = x\text{- and }y\text{- position of the target on the detector}$, or $ttt = \text{telescope tube temperature}$. Epochs are relative to the updated mean transit ephemerides given in Tables 3 (planets b , c , and d) and 4 (planets e , f , and g).

Appendix B.2: Prior distributions

Parameter (unit)	Prior
Mass, M_\star (M_\odot)	$\mathcal{N}(0.647, 0.030^2)$
Radius, R_\star (R_\odot)	$\mathcal{N}(0.662, 0.010^2)$
Effective temperature, T_{eff} (K)	$\mathcal{N}(4316, 70^2)$
Quadratic limb-darkening coefficient $u_{1,\text{CHEOPS}}$	$\mathcal{N}(0.538, 0.023^2)$
Quadratic limb-darkening coefficient $u_{2,\text{CHEOPS}}$	$\mathcal{N}(0.157, 0.033^2)$
Quadratic limb-darkening coefficient $u_{1,\text{TESS}}$	$\mathcal{N}(0.487, 0.019^2)$
Quadratic limb-darkening coefficient $u_{2,\text{TESS}}$	$\mathcal{N}(0.193, 0.047^2)$
Quadratic limb-darkening coefficient $u_{1,\text{NGTS}}$	$\mathcal{N}(0.529, 0.030^2)$
Quadratic limb-darkening coefficient $u_{2,\text{NGTS}}$	$\mathcal{N}(0.171, 0.045^2)$

Table B.2. Prior probability distribution functions assumed in our global transit analysis (see Sect. 4.1). $\mathcal{N}(\mu, \sigma^2)$ represents a normal distribution of mean μ and variance σ^2 .

Appendix C: Results: individual transit timings

Epoch	Transit timing (BJD _{TDB} - 2 450 000)	TTV (minutes)	Source
<i>TOI-178 c</i>			
-176	8356.0989 ^{+0.0080} _{-0.0138}	-2.89 ^{+11.53} _{-19.87}	TESS
-175	8359.3408 ^{+0.0061} _{-0.0050}	2.09 ^{+8.76} _{-7.21}	TESS
-174	8362.5850 ^{+0.0086} _{-0.0095}	10.29 ^{+12.43} _{-13.75}	TESS
-173	8365.8208 ^{+0.0096} _{-0.0078}	6.56 ^{+13.82} _{-11.29}	TESS
-172	8369.052 ^{+0.016} _{-0.013}	-3.38 ^{+23.47} _{-19.30}	TESS
-171	8372.308 ^{+0.011} _{-0.015}	21.06 ^{+16.42} _{-22.18}	TESS
-170	8375.5181 ^{+0.0077} _{-0.0052}	-19.55 ^{+11.10} _{-7.53}	TESS
-169	8378.7718 ^{+0.0075} _{-0.0077}	2.43 ^{+10.77} _{-11.16}	TESS
44	9068.5625 ^{+0.0104} _{-0.0086}	4.00 ^{+14.98} _{-12.40}	CHEOPS
45	9071.797 ^{+0.014} _{-0.012}	-1.78 ^{+20.74} _{-17.28}	CHEOPS
46	9075.034 ^{+0.008} _{-0.010}	-3.44 ^{+11.49} _{-14.98}	CHEOPS
51	9091.2349 ^{+0.0047} _{-0.0055}	8.67 ^{+6.78} _{-7.99}	TESS
52	9094.4701 ^{+0.0026} _{-0.0038}	3.99 ^{+3.74} _{-5.47}	TESS
53	9097.7094 ^{+0.0082} _{-0.0094}	5.20 ^{+11.88} _{-13.55}	TESS
55	9104.1840 ^{+0.0086} _{-0.0076}	1.86 ^{+12.36} _{-11.00}	TESS
56	9107.4252 ^{+0.0073} _{-0.0077}	5.81 ^{+10.56} _{-11.10}	TESS
57	9110.6629 ^{+0.0075} _{-0.0050}	4.74 ^{+10.81} _{-7.16}	TESS
63	9130.0860 ^{+0.0031} _{-0.0018}	-6.21 ^{+4.46} _{-2.62}	CHEOPS
68	9146.2850 ^{+0.0033} _{-0.0029}	3.59 ^{+4.77} _{-4.18}	CHEOPS
70	9152.7557 ^{+0.0053} _{-0.0049}	-5.30 ^{+7.70} _{-7.07}	CHEOPS
71	9155.9917 ^{+0.0089} _{-0.0097}	-8.88 ^{+12.76} _{-14.00}	CHEOPS
156	9431.2758 ^{+0.0098} _{-0.0069}	14.06 ^{+14.05} _{-9.92}	CHEOPS
176	9496.0299 ^{+0.0065} _{-0.0056}	-7.38 ^{+9.30} _{-8.02}	CHEOPS

Continued on next page

Table C.1 – *continued from previous page*

Epoch	Transit timing (BJD _{TDB} – 2 450 000)	TTV (minutes)	Source
<i>TOI-178 d</i>			
-61	8360.2385 ^{+0.0033} _{-0.0026}	-6.00 ^{+4.82} _{-3.72}	TESS
-60	8366.8025 ^{+0.0020} _{-0.0021}	2.97 ^{+2.84} _{-3.02}	TESS
-59	8373.3593 ^{+0.0040} _{-0.0082}	1.58 ^{+5.82} _{-11.88}	TESS
-58	8379.9157 ^{+0.0033} _{-0.0028}	-0.27 ^{+4.72} _{-4.02}	TESS
47	9068.4744 ^{+0.0039} _{-0.0029}	-3.27 ^{+5.63} _{-4.16}	CHEOPS
48	9075.0314 ^{+0.0039} _{-0.0055}	-4.22 ^{+5.56} _{-7.92}	CHEOPS
51	9094.7023 ^{+0.0036} _{-0.0055}	-7.51 ^{+5.13} _{-7.92}	TESS
53	9107.8186 ^{+0.0040} _{-0.0043}	-6.24 ^{+5.75} _{-6.25}	TESS
55	9120.9395 ^{+0.0012} _{-0.0013}	1.58 ^{+1.73} _{-1.83}	CHEOPS
56	9127.4973 ^{+0.0022} _{-0.0022}	1.74 ± 3.17	CHEOPS
61	9160.2843 ^{+0.0016} _{-0.0018}	-0.70 ^{+2.30} _{-2.64}	CHEOPS
<i>TOI-178 e</i>			
-40	8362.9541 ^{+0.0058} _{-0.0031}	0.07 ^{+8.29} _{-4.51}	TESS
-39	8372.9091 ^{+0.0085} _{-0.0091}	-9.80 ^{+12.25} _{-13.05}	TESS
31	9070.2469 ^{+0.0041} _{-0.0039}	5.65 ^{+5.88} _{-5.66}	CHEOPS
33	9090.1771 ^{+0.0077} _{-0.0087}	15.11 ^{+11.16} _{-12.60}	TESS
34	9100.1317 ^{+0.0016} _{-0.0014}	4.77 ^{+2.28} _{-1.96}	CHEOPS
35	9110.1036 ^{+0.0087} _{-0.0112}	19.29 ^{+12.54} _{-16.13}	TESS
37	9130.0109 ^{+0.0012} _{-0.0012}	-4.29 ^{+1.71} _{-1.70}	CHEOPS
40	9159.9040 ^{+0.0061} _{-0.0054}	6.72 ^{+8.80} _{-7.78}	CHEOPS
<i>TOI-178 f</i>			
-35	8364.9143 ^{+0.0039} _{-0.0041}	-3.41 ^{+5.57} _{-5.92}	TESS
-34	8380.1582 ^{+0.0090} _{-0.0101}	13.87 ^{+12.99} _{-14.54}	TESS
13	9096.0564 ^{+0.0056} _{-0.0051}	8.78 ^{+8.02} _{-7.39}	TESS
14	9111.2650 ^{+0.0092} _{-0.0056}	-24.86 ^{+13.31} _{-7.99}	TESS
15	9126.5155 ^{+0.0015} _{-0.0012}	1.90 ^{+2.22} _{-1.70}	CHEOPS
16	9141.7445 ^{+0.0033} _{-0.0029}	-2.36 ^{+4.74} _{-4.12}	CHEOPS
17	9156.9773 ^{+0.0016} _{-0.0015}	-1.13 ^{+2.25} _{-2.20}	CHEOPS
35	9431.1468 ^{+0.0093} _{-0.0103}	-9.23 ^{+13.35} _{-14.83}	CHEOPS
<i>TOI-178 g</i>			
-26	8354.5502 ^{+0.0038} _{-0.0041}	8.97 ^{+5.46} _{-5.89}	TESS
-25	8375.2603 ^{+0.0045} _{-0.0046}	9.30 ^{+6.51} _{-6.64}	TESS
-6	8768.7409 ^{+0.0029} _{-0.0031}	-1.81 ^{+4.18} _{-4.49}	NGTS
10	9100.0936 ^{+0.0041} _{-0.0025}	-10.13 ^{+5.93} _{-3.60}	CHEOPS
11	9120.8067 ^{+0.0018} _{-0.0014}	-5.61 ^{+2.64} _{-2.07}	CHEOPS
13	9162.2292 ^{+0.0131} _{-0.0118}	-1.65 ^{+18.86} _{-16.99}	CHEOPS
26	9431.4659 ^{+0.0020} _{-0.0022}	9.74 ^{+2.87} _{-3.18}	CHEOPS

Table C.1. Individual transit timings returned by our global transit analysis (see Sect. 4.1) for the five outer TOI-178 planets. The epochs and corresponding TTVs given here are relative to the updated mean transit ephemerides given in Tables 3 (planets *b*, *c*, and *d*) and 4 (planets *e*, *f*, and *g*).

Appendix D: Dynamical analysis: TTV mass and eccentricity posteriors for different mass priors**Table D.1.** TTV mass and eccentricity posteriors for the 5 outer planets of the TOI-178 system.

	Source	Prior	TOI-178 c	TOI-178 d	TOI-178 e	TOI-178 f	TOI-178 g
M_p [M_\oplus]	RVs (Leleu et al. 2021a)	–	4.77 ± 0.68	3.01 ± 1.03	3.86 ± 1.25	7.72 ± 1.67	3.94 ± 1.62
M_p [M_\oplus]	TTVs	<i>RV</i>	$4.70^{+0.63}_{-0.63}$	$3.35^{+0.81}_{-0.79}$	$3.11^{+0.96}_{-0.87}$	$7.50^{+1.27}_{-1.18}$	$3.12^{+1.10}_{-1.11}$
M_p [M_\oplus]	TTVs	<i>default</i>	$0.22^{+0.78}_{-0.17}$	$7.73^{+2.09}_{-1.71}$	$3.61^{+1.31}_{-1.13}$	$0.78^{+0.99}_{-0.59}$	$0.17^{+0.51}_{-0.12}$
M_p [M_\oplus]	TTVs	<i>high-mass</i>	$8.08^{+7.98}_{-5.26}$	$8.33^{+2.33}_{-2.23}$	$3.12^{+1.64}_{-1.45}$	$6.76^{+2.62}_{-2.51}$	$1.88^{+1.47}_{-1.19}$
Δ_M	Robustness criterion	–	10.08	0.29	0.37	6.06	3.34
e_p	TTVs	<i>RV</i>	$0.0073^{+0.0083}_{-0.0051}$	$0.010^{+0.011}_{-0.007}$	$0.0080^{+0.0100}_{-0.0057}$	$0.0105^{+0.0071}_{-0.0061}$	$0.0056^{+0.0058}_{-0.0039}$
e_p	TTVs	<i>default</i>	$0.0071^{+0.0081}_{-0.0050}$	$0.0051^{+0.0067}_{-0.0036}$	$0.0041^{+0.0054}_{-0.0029}$	$0.012^{+0.016}_{-0.008}$	$0.022^{+0.027}_{-0.016}$
e_p	TTVs	<i>high-mass</i>	$0.0033^{+0.0038}_{-0.0023}$	$0.0049^{+0.0055}_{-0.0034}$	$0.0050^{+0.0057}_{-0.0035}$	$0.0068^{+0.0065}_{-0.0045}$	$0.0039^{+0.0045}_{-0.0028}$